

An X-ray and Optical Investigation of the Starburst-driven Superwind in the Galaxy Merger Arp 299

T. M. Heckman

Department of Physics and Astronomy, Johns Hopkins University, Homewood Campus,
3400 North Charles Street, Baltimore, Maryland 21218

L. Armus

SIRTF Science Center, California Institute of Technology, 100-22, Pasadena, California
91125

and

K. A. Weaver and J. Wang

Department of Physics and Astronomy, Johns Hopkins University, Homewood Campus,
3400 North Charles Street, Baltimore, Maryland 21218

Received _____; accepted _____

ABSTRACT

We present a detailed investigation of the X-ray and optical properties of the starburst-merger system Arp299 (NGC 3690, Mrk 171), with an emphasis on its spectacular gaseous nebula. We analyse *ROSAT* and *ASCA* X-ray data and optical spectra and narrow-band images. The X-ray nebula in Arp 299 has a diameter of ≈ 45 kpc, is elongated roughly along the HI minor axis of the merging system, has an outer (inner) temperature of 2.3 (9) million K, a luminosity of $\sim 2 \times 10^{41}$ erg s $^{-1}$, a gas mass of $7 \times 10^9 M_{\odot}$, and a thermal energy content of $\sim 10^{58}$ ergs. An additional hard X-ray component is present with a luminosity in the 0.1 to 10 keV band of $\sim 4 \times 10^{41}$ erg s $^{-1}$ most likely due to X-ray binaries or possibly inverse Compton scattering. The overall X-ray spectrum is consistent with that of other starbursts (Dahlem, Weaver & Heckman). Compared to the X-ray nebula, the optical emission-line nebula is smaller (20 kpc) but much more luminous ($\sim 10^{44}$ erg s $^{-1} \approx 4\%$ L_{bol} for Arp 299). The kinematics of the emission-line nebula are complex, with the line-widths increasing systematically with decreasing H α surface-brightness to values of 500 to 700 km s $^{-1}$ in the faint outer filaments. The relative strengths of the low-ionization forbidden lines ([SII], [NII], and [OI]) also increase systematically as the gas surface-brightness decreases and as the line widths increase. We measure high gas pressures in the inner emission-line nebula ($P/k \sim \text{few} \times 10^6$ K cm $^{-3}$) that decline systematically with increasing radius.

We suggest that the on-going galaxy collision has tidally-redistributed the ISM of the merging galaxies. The optical emission-line nebula results as this gas is photoionized by radiation that escapes from the starburst, and is shock-heated, accelerated, and pressurized by a ‘superwind’ driven by the collective effect of the starburst supernovae and stellar winds. Since empirically

only those galaxy mergers that contain luminous starbursts have bright X-ray nebulae, this implies that the luminous X-ray nebula in Arp 299 is also powered by the starburst outflow (rather than by the collisions of gas clouds during the merger). This outflow can be most directly traced by its X-ray emission, which is plausibly a mass-loaded flow ($\sim 10^2 M_{\odot} \text{ yr}^{-1}$) of adiabatically-cooling gas that carries out a substantial fraction of the energy and metals injected by the starburst at a speed close to the escape velocity from Arp 299. The mass outflow rate exceeds the star-formation rate in this system. We conclude that powerful starbursts are able to heat (and possibly eject) a significant fraction of the interstellar medium in galaxies that are the products of mergers.

Subject headings: galaxies: individual (Arp 299, NGC 3690, Mrk 171) – galaxies: starburst – galaxies: interactions – galaxies: ISM – X-rays: galaxies

1. Introduction

1.1. General Motivation

Galaxies that emit the bulk of their luminosity in the far-infrared (hereafter far-IR galaxies) are an energetically significant component of the local universe (e.g. Soifer et al 1987; Sanders & Mirabel 1997). They are also the only local systems (apart from QSOs) that have bolometric luminosities similar to typical high-redshift galaxies selected by UV (Steidel et al 1996; Meurer, Heckman, & Calzetti 1998) or sub-millimeter (e.g. Hughes et al 1998; Blain et al 1998) techniques. As such, they offer unique laboratories to study the physical processes that were important in the formation and early evolution of galaxies (Heckman 1998).

One of their most interesting attributes are their galactic-scale and highly luminous gaseous emission-line nebulae (cf. Armus, Heckman, & Miley 1990; Veilleux et al. 1995). In several well-known cases like M 82 and NGC 253, hot X-ray emitting gas has also been discovered, and this gas shows a clear morphological relationship to the optical emission-line nebula (cf. Dahlem, Weaver, & Heckman 1998 and references therein).

It seems clear in these cases that the X-ray nebulae are energized by the mechanical energy of an outflow driven by the multiple supernovae in the starburst (a ‘superwind’ — cf. Heckman, Lehnert, & Armus 1993; Bland-Hawthorn 1995). It would be important to establish the ubiquity of the superwind phenomenon in far-IR galaxies, since such outflows could play an important role in heating and chemically-enriching galactic halos and the inter-galactic medium (cf. Heckman, Armus, & Miley 1990; Gibson, Loewensten, & Mushotzky 1997).

The X-ray nebulae studied in detail and at high spatial resolution to date have been mostly associated with far-IR galaxies of modest luminosity ($L < \text{few} \times 10^{10} L_{\odot}$). The

situation may be different and more complex for more powerful far-IR galaxies. These systems are also primarily powered by intense starbursts (Genzel et al 1998), and are created in the aftermath of a galactic collision or merger (cf. Mihos & Hernquist 1994), so that the dissipation of the kinetic energy of the colliding interstellar media may be energetically significant (Harwit et al. 1987). It is also particularly interesting to study the effects of possible superwinds on the interstellar media of merging disk galaxies in general, since such hydrodynamical processes may be important in the subsequent transformation of the merger product into an elliptical galaxy (e.g. Schweizer 1992).

We have therefore undertaken an analysis of X-ray and optical data for a small sample of some of the nearest and brightest powerful infrared galaxies ($L_{FIR} \geq 10^{45}$ erg s⁻¹) in order to determine the characteristics of their nebulae and thereby determine the nature of their energy sources. Heckman et al. (1996) presented X-ray and optical data on the prototypical ‘ultraluminous’ far-IR galaxy Arp 220, and showed that this galaxy appears to have an outflow that is qualitatively similar to (but more powerful than) the outflows seen in M 82 and NGC 253. In Wang et al. (1997), we reported the results for the case of Mrk 266, and here we discuss a third example. Iwasawa & Comastri (1998) have recently reported on the X-ray properties of the IR-bright merger system NGC 6240.

Our approach is complementary to the recent work by Read & Ponman (1998), who have systematically studied the X-ray properties of an optically- selected sample of merging galaxies using *ROSAT* data. The members of their sample are not in general powerful starbursts, and only Arp 220 meets the above far-IR luminosity criterion.

1.2. Arp 299

The powerful far-IR system Arp 299 (also known as NGC 3690 and Mrk 171) consists of two overlapping galaxies that appear to be in the late stages of a merger.^{1 2} It has one of the brightest, most luminous, and largest emission-line nebulae in the extensive H α imaging survey of far-IR galaxies by AHM90. As we will describe in this paper, this material is immersed in and surrounded by a large and bright region of soft X-ray emission. Arp 299 is therefore a prime target for a detailed examination of the relationship between the warm and hot gaseous components in powerful far infrared galaxies.

Arp 299 has been extensively studied following the landmark paper of Gerhez, Sramek, & Weedman (1983): in the X-ray (Zezas, Georgantopoulos, & Ward 1998 - hereafter ZGW), UV (Meurer et al 1995), IR (Fischer et al 1983; Telesco, Decher, & Gatley 1985; Beck et al 1986; Nakagawa et al 1989; Joy et al 1989; Wynn-Williams et al 1991), and radio (Condon 1991) wavebands, and in HI (Stanford & Wood 1989 ; Hibbard 1997), OH (Baan & Haschick 1990), CO (Aalto et al 1997; Sargent & Scoville 1991), and HCN (Aalto et al 1997). It has been the site of several recent supernovae (SN1992bu - IAU Circular 5960; SN1993G - IAU Circular 5718; SN1998T - IAU Circular 6859; and a possible radio supernova described

¹In most past papers on this system, the Eastern member of the merging galaxy pair has been designated IC 694 and the Western member as NGC 3690. However, as pointed out in IAU Circular 6859, IC 694 is properly the designation of a small E/S0 galaxy located about 1' to the northwest of the merging galaxy pair, while NGC 3690 properly refers to the merging pair. To avoid further confusion, we will adopt the name Arp 299 to refer to the system rather than NGC 3690.

²In this paper, we will adopt a distance to Arp 299 of 44 Mpc, derived using the linear Virgocentric infall model described in Marlowe et al. (1995) and a far-field value of $H_0 = 75 \text{ km s}^{-1} \text{ Mpc}^{-1}$. This implies a scale of $1'' = 0.21 \text{ kpc}$ and $1' = 13 \text{ kpc}$.

in IAU Circular 4988). Arp 299 has a bolometric luminosity of approximately $6 \times 10^{11} L_{\odot}$, which is dominated by far-IR emission. The centers of the two merging galaxies are separated by only about $22''$ (4.5 kpc in projection), with a clear overlap in the disks. Following the nomenclature of Gerhez, Sramek, & Weedman (1983), the compact site of activity in the central region of the Eastern galaxy is denoted 'A', while the activity in the Western galaxy breaks up into a complex of sources (a double source "B1", and "B2" the first of which is evidently associated with the nucleus of the galaxy, and a third source "C" roughly $8''$ or 1.6 kpc NNW of B1).

In the present paper we present an analysis of both X-ray and optical imaging and spectroscopy of Arp 299. Our approach complements that of ZGW, who analyzed the PSPC spectrum, but not the morphological structure of the *ROSAT* data. Our data analysis is described in §2 and the results for X-ray and optical data are presented in §3 and §4 respectively. We will discuss and interpret these results in §5 in an attempt to determine how the bright optical/X-ray nebula is heated and how Arp 299 and its nebula may fit in to the general class of powerful far-IR galaxies. In §6 we will summarize our conclusions.

2. Observations and Data Reduction

2.1. X-ray Imaging and Spectroscopy

Arp 299 has been observed in the soft and medium-energy X-ray bands with the Rontgensatellit (*ROSAT*) and the Advanced Satellite for Cosmology and Astrophysics (*ASCA*; Tanaka, Inoue & Holt 1994). *ROSAT* contains the high-resolution soft X-ray imaging detector (HRI) and the positional sensitive proportional counter (PSPC), while *ASCA* contains two sets of detectors which are the solid-state imaging spectrometers (SIS; designated here as S0 and S1) and the gas imaging spectrometers (GIS; designated S2 and

S3). The data from the two satellites are complementary. For soft X-rays (0.1 – 2.0 keV), *ROSAT* provides $\sim 5''$ spatial resolution with the HRI and moderate spectral resolution with the PSPC. The *ASCA* instruments extend the spectral coverage to 10 keV with a factor of ten better spectral resolution (albeit with poor spatial resolution). The X-ray data were obtained by us (*ROSAT*) and from the HEASARC³ operated by the LHEA⁴ at the Goddard Space Flight Center (*ASCA*).

The *ROSAT* HRI observations occurred on April 13 – 14 1992 for a total live time integration of 6691 seconds. The nominal pointing center of the HRI was 11h:25m:42.8s, +58d:50m:15s, which places the center of the HRI field of view at a position approximately halfway between the interacting galaxies that comprise Arp 299. The HRI background is approximately constant over the field of view and so we subtract a constant offset, which is determined by averaging the background at different source-free locations. After background subtraction, there are 285 counts in the HRI image, corresponding to a count rate of 0.0426 cnt s⁻¹ from Arp 299. For imaging analysis, the data were binned and smoothed with a Gaussian having $\sigma = 3''$, yielding an effective resolution of 7'' FWHM.

Arp 299 was observed with the PSPC in multiple intervals from 1991 November 19 to 1993 April 23 for 9,925 net seconds. Times of a high master veto rate (MVR above ~ 220) indicating charged particle contamination were negligible, and so we include all of the on-source data in our analysis. After correcting for vignetting and subtracting background, the PSPC count rate for Arp 299 is 0.10 counts s⁻¹, yielding 983 counts.

ASCA observed Arp 299 on April 16 and December 1 1994 for ~ 6 and ~ 36 ks, respectively. The first data set provides few source counts and so we examine only the

³The high energy astrophysics data archive at <http://heasarc.gsfc.nasa.gov/>

⁴The Laboratory for High Energy Astrophysics.

data from the second observation. To remove times of high background, we selected data within time ranges defined by the following criteria: for the SIS, the satellite was required to be outside the SAA with an Earth elevation angle greater than 10° and a geomagnetic cutoff rigidity (COR) greater than 6 Gev c^{-1} . In addition, we removed times less than 16 s after an SAA passage, 60 s after a day-to-night passage, and during times of Bright Earth when the elevation angle was less than 20° . For the GIS, the satellite was required to be outside the SAA with an Earth elevation angle greater than 5° and a geomagnetic cutoff rigidity (COR) greater than 6 Gev c^{-1} . Two background spikes were also removed. Remaining on-source times were 26.3 ks (S0), 28.3 ks (S1) and 36.2 ks (G2 and G3). The background during the observation ranged from 20 to 30% of the total count rate from 1 – 10 keV. Source spectra were extracted by selecting circular regions of $\sim 3'$ radius and background was selected from near the source in the GIS and from the same chip in the SIS. The background-subtracted count rates are 0.042, 0.039, 0.023, and 0.033 counts s^{-1} , for S0, S1, S2, and S3, respectively (totalling 4,234 source counts).

To extract *ROSAT* images and spectra we use the IRAF/PROS V2.3.1 data reduction package. For *ASCA* we use FTOOLS v4.0. With the exception of the spatially-resolved halo emission in the PSPC, all spectra are grouped to have ≥ 15 counts per bin to allow the use of χ^2 statistics. There are too few counts in the halo to assume a Gaussian probability distribution and so Poisson errors and the C-statistic (Cash 1979) are used for spectral modeling.

2.2. Optical Spectroscopy

Optical spectra of the Arp 299 system were obtained in May 1987 and January 1988 using the KPNO 4-meter Mayall telescope in combination with the RC spectrograph and a TI2 CCD. The May 1987 data (hereafter May87) are of medium spectral resolution

(3.6\AA Full Width Half Maximum - FWHM) and cover the wavelength range of 6000-7000 \AA . Three slits ($2.0'' \times 3.0'$) were placed at a position angle (PA) of 90° along the Arp 299 system. Two of these slits intercept components "C" and "B"1 respectively (in the notation of Gehrz, Sramek, & Weedman 1983). The third slit was placed to be parallel to the first two, but displaced $24''$ north of component "C". The January 1988 data (hereafter Jan88) are of low resolution (13.5\AA FWHM) and cover the wavelength range of 4200-7000 \AA . The slit dimensions were the same as those used for the May87 data., but here the slits were placed to intercept component "A" (at a PA= 90°) and to pass along the tail of emission to the northwest of Arp 299 (at a PA= 120°). Both the May87 and the Jan88 data were binned by a factor of 2.0 in the spatial direction to achieve a pixel scale of $0.89''$ pixel $^{-1}$.

The May87 and Jan88 spectra were bias-subtracted and flat-fielded using the NOAO's IRAF software. The LONGSLIT package was used for wavelength calibration and distortion correction of the raw spectra. Only the low resolution spectra (Jan88) were taken under photometric conditions, and these were flux-calibrated in IRAF using KPNO IIDS standard stars. For each extracted spectrum, the SPLOT package was used to measure the integrated line fluxes, central wavelengths, linewidths, equivalent widths and continuum levels. The $\text{H}\alpha$ + $[\text{NII}]$ complex was deblended in the data by requiring the widths of the lines to be the same. The $[\text{SII}]$ lines at 6717\AA and 6731\AA were required to have the same linewidth and, in regions of low signal to noise, to have a fixed wavelength separation of 14.6\AA . In all cases, the uncertainties in the line fits were estimated as a function of signal-to-noise ratio by comparing the measured value of the $[\text{NII}]\lambda\lambda\ 6584\text{\AA}/6548\text{\AA}$ flux ratio to that of the value of 3.0 expected from atomic physics.

3. Results

3.1. X-Ray Morphology

3.1.1. *ROSAT* PSPC

The background-subtracted 0.1 – 2.4 keV PSPC image of Arp 299 is shown superimposed on the Palomar Sky Survey image in Figure 1. Accurate astrometry is not possible for the PSPC because no independent X-ray point sources are present in the field of view, and so the image is aligned with the optical centroid of the Arp 299 system to within the accuracy of the *ROSAT* pointing uncertainties ($\sim 4 - 6''$).

In order to investigate the morphology of the X-ray image as a function of energy, we constructed “soft” band (0.1 – 0.5 keV) and “hard” band (0.5 – 2.4 keV) images. Photons were selected from the appropriate pulse invariant (PI) channels and the central $6.17'$ by $6.17'$ regions were extracted from the original unbinned X-ray map ($0.5''$ pixels). These images were then smoothed with a Gaussian function with $\sigma = 30$ pixels ($35''$ FWHM). After smoothing, the images were shifted slightly to align the center of the hard *ROSAT* image (which represents the core of X-ray emission from the galaxy) with the center of emission mapped with the HRI (see below).

The PSPC images, shown in Figure 2, reveal that the hard and soft X-ray isophotes are elongated in nearly orthogonal directions. The hard X-ray image is more compact, possibly oriented in the east-west direction (no doubt resulting from the complex of point sources seen in the HRI data). The soft X-ray isophotes on the other hand, are clearly oriented in the NNE/SSW direction, and are extended on a scale of $\sim 3.5'$, or 45 kpc. The size of the soft X-ray emission is similar to that of the HI mapped by Stanford & Wood (1989), but the X-ray emission is roughly perpendicular to the NW/SE orientation of the HI. The shapes of the soft-band and hard-band images imply at least two distinct emission regions.

3.1.2. *HRI*

The HRI image (Fig. 3) has a total background-subtracted count rate of 0.0426 cts s^{-1} , and shows a complex, clearly resolved structure extended over more than an arcminute in a predominantly east-west direction. This is the direction of the two galaxies in the interacting system. There are numerous local maxima in the X-ray image, but the brightest source to the east is only $\sim 10''$ north of the non-thermal radio and near-infrared nucleus of the Eastern galaxy (Gehrz, Sramek & Weedman 1983; Condon 1991; Wynn-Williams, et al. 1991). This is nucleus “A” in the nomenclature of Gehrz, Sramek & Weedman (1983). Given the pointing accuracy of the *ROSAT* and the fact that nucleus A is the single primary peak in both the radio and near infrared data, we hereafter identify the eastern X-ray peak with nucleus A. The western X-ray peak is extended in a “ridge” of emission with two prominent knots separated by 4 to 5 ". When the eastern peak is aligned with nucleus “A”, the southeast knot in the ridge is coincident with component “B1” and the northwest knot appears to be associated with a bright knot of $H\alpha$ emission a few " to the west of component “B2”. Note that while B1 is the peak in the 2.2 micron, 10 micron, and radio emission in the Western galaxy, “B2” is the optical continuum peak. Finally, the infrared and radio peak known as component “C” is not located at the position of a relative peak in the *ROSAT* HRI image (a weak X-ray source tabulated by ZGW is located about 5" to the NW of C). Thus, although component “C” is a source of optical, near-infrared and radio emission, it does not appear to be a strong source of X-rays.

We can estimate the contribution of point sources to the total number of counts in the HRI image by summing the flux from the three strongest point sources within 5" square apertures (a “detection cell” that includes 50% of the total flux expected from a point source). These three X-ray sources are equally bright (to within $\pm 10\%$) and together account for approximately 21% of the total counts in the HRI image, after correction for the

50% of the flux beyond the 5'' detection cells (0.0087 counts s⁻¹). Although the HRI data do not provide much spectral information, we can estimate their fluxes and luminosities over 0.1 – 2.4 keV range by assuming a simple spectral model (David et al 1997). If the point sources are modelled as a MEKAL plasma with kT = 0.8 keV (see §3.2.2) and line of sight neutral HI column of $N_H = 10^{20} \text{ cm}^{-2}$ ($N_H = 5 \times 10^{21} \text{ cm}^{-2}$), they have a combined unabsorbed X-ray luminosity of about $0.6 \times 10^{41} \text{ erg s}^{-1}$ ($2.2 \times 10^{41} \text{ erg s}^{-1}$) from 0.1 – 2.4 keV. Alternatively, if the point sources are modelled as having power law spectral shapes with a photon index of 1.6 (the index of the hard X-ray component - see §3.2.3) they have a combined X-ray luminosity of $1.0 \times 10^{41} \text{ erg s}^{-1}$ ($3.1 \times 10^{41} \text{ erg s}^{-1}$) from 0.1 – 2.4 keV.

Each of the three sources thus has a luminosity in the 0.1 to 2.4 keV band of $\sim \text{few} \times 10^{40}$ to $10^{41} \text{ erg s}^{-1}$. This can be compared to the most powerful individual X-ray sources known in nearby galaxies, which have peak X-ray luminosities of $\sim 10^{40} \text{ erg s}^{-1}$: SN1978C in NGC 1313 (Ryder et al 1993), SN1986J in NGC 891 (Bregman & Pildis 1992), SN 1993J in M 81 (Zimmermann et al 1994; Kohmura et al 1994), and the highly variable sources in the nuclei of M 82 (Collura et al 1994) and NGC 3628 (Dahlem, Heckman, & Fabbiano 1995). It is worth emphasizing that at the distance of Arp 299, 5'' corresponds to roughly 1 kpc, and that the sources are coincident with the sites of the most intense star-formation in Arp 299. Higher resolution X-ray imaging with AXAF may well resolve these sources into multiple sub-components.

3.2. X-ray Spectra

The different morphologies of the hard and soft-band PSPC images suggest that there are at least two sources of X-rays in the Arp 299 system with different spectral shapes and possibly different emission mechanisms. To uncover these emission mechanisms we extract spatially-resolved spectra from the central and outer regions. The central or “core” region

is defined with a circle of diameter = $1.3'$ centered on the X-ray peak of Fig. 2a. The outer or “halo” region is defined with an ellipse having a major axis = $2.78'$, minor axis = $2.22'$, and P.A. = 193° centered on the X-ray peak of Figure 2a. Background is taken from source-free regions near the galaxy. The extraction regions, source counts and count rates are listed in Table 1 and the spatially-resolved halo and core spectra are shown in Figure 4.

3.2.1. *The Halo Spectrum*

There are 328 counts from within the halo region, 119 of which are source counts and 209 (almost 2/3) of which are background counts. We estimate the contribution of background counts to the total spectrum by calculating the areas of the halo and background regions and then using the ratio of areas to predict the contribution of background in the halo region. We then determine an empirical spectral model for the background and include this model (properly normalized) in our spectral fits to “subtract” the background contribution. Our empirical background model consists of a power law with $\Gamma = 2.3 \pm 0.2$ and an unresolved Gaussian-shaped emission line at 0.53 keV. The line represents oxygen fluorescence from Earth’s atmosphere and the power law approximates contributions from the particle background and diffuse X-ray background, as well as long-term and short-term enhancements in the background rate.

The statistics are too poor to distinguish between different physical models for the halo emission. In particular, the data cannot distinguish between the two most natural choices, which are a power-law spectrum (where the X-rays are produced by inverse-Compton scattering of lower energy photons) and a thermal spectrum (where the X-rays are produced in a plasma that has been heated by shocks). A power-law spectrum is expected if the soft X-rays result from emission associated with an extended synchrotron-emitting radio halo, such as that found around M82 (Seaquist & Odegard 1991). However, the radio emission

in Arp 299 is not extended on the same scale as the soft X-rays (Condon et al. 1990). In fact, the soft X-ray emission is extended in a direction (North-South) that is roughly perpendicular to the radio source major axis. This implies that the X-ray emission is not related to the emission at radio wavelengths in Arp 299, and hence a power-law description of the halo is unlikely. Recent studies of extended emission in starburst galaxies indicate that the soft emission is primarily thermal (see Dahlem, Weaver & Heckman 1998) and so we choose a model that consists of an emission spectrum from hot, diffuse gas based on calculations by Mewe and Kaastra with Fe L calculations by Liedahl (Mewe, Gronenschild & van den Oord 1985; Mewe, Lemen & van den Oord 1986; Kaastra 1992 - hereafter referred to as the MEKAL model).

When the data are fitted with a single temperature MEKAL model and solar abundances are assumed, we find no evidence for absorption in excess of the Galactic column density ($0.9 \times 10^{20} \text{ cm}^{-2}$; Burstein & Heiles 1982), and the spectrum is well described with a plasma having $kT = 0.20_{-0.07}^{+0.12} \text{ keV}$ (Table 2). The 0.1 – 2.4 keV unabsorbed flux for this model is $2.8 \times 10^{-13} \text{ ergs cm}^{-2} \text{ s}^{-1}$, corresponding to a halo luminosity of $\sim 7 \times 10^{40} \text{ erg s}^{-1}$.

3.2.2. *The Core Spectrum*

For the core spectrum, a single-component power-law model yields a poor fit (Table 2; Model A) and results in positive residuals near 0.9 keV that resemble a blend of primarily Fe L and Ne line emission (Figure 5a). MEKAL plasma models with solar abundances also yield poor fits (Table 2; Models B1 and B2), even when the absorbing column density is a free parameter in the fit. This can be seen in Figure 5b, which shows evidence for excess flux toward higher energies. If the abundance is allowed to vary, the fit improves (Table 2; Model B3) implying an abundance of $0.12(+0.10 -0.06)Z_{\odot}$. Such a low abundance seems

highly unusual, especially in light of the intense starburst in Arp 299, but since abundance calculations are derived from line equivalent widths, the possibility exists that a second thermal or hard X-ray component (not uniquely detectable with the PSPC) may contribute continuum flux at low energies. Such a component would dilute the line emission from the plasma and cause the abundance of the hot gas to be underestimated. This behavior is typical of starburst spectra that intrinsically contain multiple emission components but are fitted with single-component plasma models (Dahlem, Weaver, & Heckman 1998; Weaver, Heckman, & Dahlem 1998). For the remainder of this paper we therefore assume that the X-ray emitting gas has solar abundance.

For the case of solar abundances, the PSPC data require at least two spectral components. Models that consists of a medium-temperature MEKAL plasma and a thermal bremsstrahlung with $kT = 7.0$ keV (Table 2; Model C) or a medium-temperature MEKAL plasma and a power law with $\Gamma=1.7$ (not shown) provide excellent fits as long as the column density is allowed to be about 2 to 3 times larger than the Galactic value. In this case, $kT \sim 0.7$ keV for the medium-temperature plasma. The ratio of the core spectrum to the two-component MEKAL plus bremsstrahlung model is shown in Figure 5c. The 0.1 – 2.4 keV unabsorbed flux for this model is 1×10^{-12} ergs cm $^{-2}$ s $^{-1}$, corresponding to a core luminosity of $\sim 2.3 \times 10^{41}$ erg s $^{-1}$.

3.2.3. Joint PSPC plus ASCA fits (0.1 – 10 keV)

ASCA cannot spatially resolve the X-ray emission and so we use the integral PSPC spectrum for joint fits. The spectral coverage to ~ 10 keV provided by *ASCA* allows us to detect a distinct hard X-ray component. Single power-law or MEKAL plasma models provide extremely poor fits to the *ASCA* plus PSPC spectrum (Table 3; Models A and B). Note that this is true even if the abundance is a free parameter in the fits. The ratio of

the joint data to the MEKAL model (Figure 6) clearly illustrates both excess line emission near 0.9 keV and a high energy excess beyond about 5 keV. A two-component MEKAL plus power-law model provides the best fit (Model C) but the MEKAL temperature is higher than that found for the halo (§3.2.1) and the derived abundances are sub-solar. The abundances can be reconciled with solar if we add to the model the 0.2 keV MEKAL plasma component found in the halo (Model D). In this case, the hard X-ray component requires absorption in excess of the Galactic value.

We note that our approach and results differ somewhat from ZGW who also fit the joint *ASCA* plus PSPC spectrum. They did not require our soft (0.2 keV) component, nor did they find evidence for intrinsic absorption. The inclusion of the soft component in our model fits is dictated primarily by our spatial analysis of the PSPC image as a function of energy (which ZGW did not undertake). Our analysis demonstrates that the soft 0.2 keV component is definitely present in the halo (and hence must be incorporated in the global fit to the *ASCA* plus PSPC spectrum). As described in the previous paragraph, inclusion of the 0.2 keV component then leads to higher values of N_H for the hard component. This nicely illustrates the power of combining all the available information provided by the X-ray images and spectra when interpreting the complex X-ray emission from starbursts.

The data and best-fitting three component model (Model D) are shown together in Figure 7 and the deconvolved model is shown at full resolution in Figure 8. The goodness of the fit is illustrated by the ratio of the data to the best-fitting model (Model D) in Figure 9. In addition to the 0.2 keV halo component, the second thermal component has a temperature of 0.77 keV, and the hard component is well represented as either a power-law with photon index 1.6 or thermal bremsstrahlung emission with $kT \sim 11$ keV.

The intrinsic column of HI in Model D (of-order 10^{21} cm $^{-2}$) is similar to that inferred from the dust extinction measured in our optical spectra (see section 4.2 below). The

unabsorbed fluxes for the $0.1 - 2.4$ keV and $2 - 10$ keV bands are $\sim 1.4 \times 10^{-12}$ erg cm $^{-2}$ s $^{-1}$ and $\sim 1.1 \times 10^{-12}$ erg cm $^{-2}$ s $^{-1}$, respectively (Table 4). The corresponding X-ray luminosities are 3.3×10^{41} erg s $^{-1}$ and 2.5×10^{41} erg s $^{-1}$.

3.2.4. *The Nature of the Hard Component*

We will discuss the nature of the two MEKAL plasma components extensively in sections 3.3 and 5.2 below. Here we remark that the hard (powerlaw or bremsstrahlung) component is most likely due to a combination of inverse Compton scattering of soft starburst photons by the relativistic electrons responsible for the radio synchrotron emission (see Moran & Lehnert 1997) and a population of X-ray binaries. Comparing the flux of this hard component in the energy band of the *ROSAT* HRI to that of the ensemble of bright point sources seen in the HRI image we find that they are similar. The absorption-corrected $0.1 - 2.4$ keV flux of the hard X-ray component is $\sim 7 \times 10^{-13}$ ergs cm $^{-2}$ s $^{-1}$ (Table 4). The HRI flux from the three brightest point sources (having a combined count rate of 0.009 counts s $^{-1}$) is $\sim 1 - 1.3 \times 10^{-12}$ ergs cm $^{-2}$ s $^{-1}$ for $N_{\text{H}} = 2.6 - 7.2 \times 10^{20}$ cm $^{-2}$ (Table 3). The hard component seen with *ASCA* could thus account for most of the flux from the bright point sources in the HRI image.

An identification of the hard component with the three bright point-like sources seen in the HRI bandpass (~ 1 keV) then argues strongly against the hardest ($E \geq 3$ keV) X-rays being dominated by emission from a heavily absorbed AGN (both on morphological grounds, and because a heavily absorbed source would produce too few counts in the HRI band). The point-like nature of the HRI sources also argues against inverse Compton scattering from a diffuse population of radio-synchrotron-emitting electrons. Instead, emission from a population of high-mass X-ray binaries is most likely (as ZGW conclude on independent grounds).

3.3. Physical Parameters of the X-Ray Gas

The joint *ROSAT* plus *ASCA* X-ray spectrum of Arp 299 requires a multi-component fit, as outlined in section 3.2. In addition, the different morphologies of the hard and soft PSPC images suggest that these spectral components are dominant over different spatial regions in Arp 299. The soft, cooler X-ray gas appears to be more extended than the hard, hotter X-ray gas (see Fig. 2). In order to derive the physical parameters of the X-ray gas and compare them with those predicted from models of a superwind, we must estimate the appropriate volumes for the soft and hard spectral components. In the calculations that follow, we assume the hard, 0.77 keV thermal plasma occupies a region of 1.3' radius (our extraction region for the core spectrum), corresponding to a volume of $5.8 \times 10^{68} \text{ cm}^3$. The soft, 0.20 keV plasma is assumed to occupy a volume of $3.5 \times 10^{69} \text{ cm}^3$, equivalent to the volume enclosed by the “total” spectrum described in section 3.2.3. We have divided this volume into core and halo components, as in section 3.2, in order to derive gas parameters for the soft thermal component. The emission integral (the volume integral of the density squared) for the soft component is $1.6 \times 10^{64} \text{ cm}^{-3}$, 60% of which is contained within a radius of 1.3', the boundary of the extracted core spectrum. If the volume filling factor of the X-ray gas is f , where $f \leq 1$, the physical parameters of the soft thermal component can be estimated:

1. The mean core gas density is $4 \times 10^{-3} f^{-1/2} \text{ cm}^{-3}$. The mean halo gas density is $1.5 \times 10^{-3} f^{-1/2} \text{ cm}^{-3}$.
2. For $T = 2.3 \times 10^6 \text{ K}$, the corresponding pressures are $2.5 \times 10^{-12} f^{-1/2} \text{ dyne cm}^{-2}$ for the core gas and $1 \times 10^{-12} f^{-1/2} \text{ dyne cm}^{-2}$ for the halo gas.
3. The mass of the gas at $T = 2.3 \times 10^6 \text{ K}$ in the core is $1.9 \times 10^9 f^{1/2} M_{\odot}$. The mass of gas at this temperature in the halo is $3.5 \times 10^9 f^{1/2} M_{\odot}$.

4. The thermal energy contents of the core and halo components are $2.2 \times 10^{57} f^{1/2}$ erg and $4 \times 10^{57} f^{1/2}$ erg, respectively.
5. The radiative cooling times are $2 \times 10^8 f^{1/2}$ yrs and $6 \times 10^8 f^{1/2}$ yrs, for the core and halo gas, respectively. Here, we have used $t_{cool} = 3kT(\Lambda n)^{-1}$, where $\Lambda = 3.5 \times 10^{-23}$ erg cm³ s⁻¹ (Sutherland & Dopita 1993) for gas at solar abundances at these temperatures.

We can similarly calculate the physical parameters for the second MEKAL thermal plasma identified in the spectrum of Arp 299 by our joint *ROSAT* plus *ASCA* spectral fits. For a volume integral of the density squared of this second, hard thermal plasma at $kT=0.77$ keV of 3.7×10^{63} cm⁻³, the physical parameters of this hot gas are:

1. The mean gas density is $2.5 \times 10^{-3} f^{-1/2}$ cm⁻³.
2. The corresponding pressure is $6.3 \times 10^{-12} f^{-1/2}$ dyne cm⁻².
3. The mass of gas at $T=9 \times 10^6$ K is $1.2 \times 10^9 f^{1/2} M_{\odot}$.
4. The thermal energy content of the gas is $5.5 \times 10^{57} f^{1/2}$ erg.
5. The radiative cooling time of the gas is $1.3 \times 10^9 f^{1/2}$ yrs for solar metallicity (Sutherland & Dopita 1993).

4. Optical Spectra

The long slit optical spectra can provide a wealth of details on the physical conditions of the warm ($T \sim 10^4$ K) ionized gas in the Arp 299 system. The temperature, density, pressures, and excitation state of this gas can in turn help constrain models of a starburst-driven outflow. The May87 and Jan88 slits are shown superimposed on the H α image of Arp 299 in Fig. 10. The overall size of the emission-line nebula is approximately 20 kpc.

As an illustration of the diversity in the emission-line properties seen across the Arp 299 nebula, we have extracted seven, one-dimensional spectra covering the $6300\text{\AA} - 7000\text{\AA}$ wavelength range from various locations in the nebula which we feel are representative of the data set as a whole. All seven spectra are from the medium resolution May87 data set, and are presented in Figs. 11a-g. The first two spectra (Fig. 11a, b) are centered on components “B1” and “C”, respectively, while the third spectrum (Fig. 11c) is from a region approximately $2''$ north of component “A”. In Figs. 11a-c the spectra have been generated by summing $4.5''$ along the appropriate slit. The fourth spectrum (Fig. 11d) has been generated by summing along a region $10''$ in length located $11''$ east of component “C” in the May87 longslit data. Figures 11e, f, and g are spectra extracted from regions well removed from the galaxy nuclei, and are chosen to show the strong [NII], wide lines, and $H\alpha$ line splittings which characterize the faint gas in the outer portions of the Arp 299 system (see the figure caption for a description of the location of each of these spectra in the nebula).

In the following sections we describe the physical state of the optical emission-line gas surrounding the two galaxy nuclei.

4.1. Gas Densities and Pressures

We have used the medium resolution May87 data to calculate the electron density as a function of radius from components A, B, and C by measuring the [SII] $\lambda\lambda 6717/6731$ line flux ratio. For the Western half of the emission-line nebula, the geometric center of sources B and C is used to calculate the radial distances for the plot of density vs. radius shown in figure 12. Although there are large errors associated with some of the points beyond 1 kpc from the nuclei, it is clear from this plot that the density drops with radius from a peak of about 250 cm^{-3} to the low density limit ($\approx 50\text{ cm}^{-3}$) at radii of a few kpc.

Assuming that the temperature in SII zone is roughly 10^4 K (as appropriate for either photoionized or shock-heated gas - cf. Dopita & Sutherland 1996), the corresponding thermal pressures are $P/k \sim 5 \times 10^6$ K cm $^{-3}$ in the inner region dropping below $P/k \sim 1 \times 10^6$ K cm $^{-3}$ beyond a radius of a few kpc.

4.2. Extinction

From the low resolution Jan88 data, we are able to measure the Balmer decrement as a function of position along both slits. These measurements are converted to extinction measurements at $H\beta$ assuming an intrinsic $H\alpha$ -to- $H\beta$ line flux ratio of 2.86 and the interstellar extinction curves of Mathis (1990). Along the PA=90 slit, the extinction peaks at nucleus A, yet is at a relative minimum to the south of C (recall that this slit does not pass directly through component C). At the location of component A, $H\alpha/H\beta = 7.1$, corresponding to 1.9 mag of extinction at $H\alpha$. However, 2.3" south of C the extinction at $H\alpha$ is only about 0.3 mag. Between nuclei A and B, the extinction is approximately 1.2 – 1.4 mag at $H\alpha$. Along the PA=120 slit, to the northwest of nucleus B, the $H\alpha$ -to- $H\beta$ line flux ratios imply extinctions at $H\alpha$ of only 0.2 – 0.7 mag. Dust is obscuring the gas directly east of component A where the extinction at $H\alpha$ is greater than 1.3 mag. Although component A has the largest amount of foreground extinction in the Arp 299 system, the regions between A and C (at the interface of the two interacting galaxies) also appear to be heavily reddened, with extinctions at $H\alpha$ of 0.7 – 1.3 magnitudes, steadily decreasing westward from component A. The PA=120 Jan88 spectrum shows that the outer regions of the system have relatively low extinction compared to the nuclei, with less than 0.7 magnitude at $H\alpha$ at radii 12 to 20 arcsec northwest of component C.

Gehrz, Sramek and Weedman (1983) measure an $H\alpha/H\beta$ line flux ratio of 5.5 at the position of component C through a 3.6" aperture, which is equivalent to an extinction of

1.4 mag at $H\alpha$. Stanford & Wood (1989) measure HI column densities of 8.6×10^{21} and $3.1 \times 10^{21} \text{ cm}^{-2}$ respectively at the locations of components A and C, corresponding to extinctions at $H\alpha$ of about 4.3 mag and 1.5 mag, respectively. Although the lower values we see for extinction near component C as compared to Gehrz et al. and Stanford & Wood can be explained if the reddening is strongly peaked at C, the differences between our measured value at A and the HI results cannot be explained this way since our slit passed directly over component A. The neutral hydrogen column densities implied by the Balmer decrement are about half as large as those measured by Stanford & Wood. This disagreement is not surprising, since both estimates depend upon uncertain assumptions: the optically-derived columns assume a normal Galactic dust-to-gas ratio and the radio-derived columns are directly proportional to the assumed HI spin temperature.

We conclude that the extinction in Arp 299 is quite inhomogeneous. For the purposes of the discussion to follow we will adopt a net extinction at $H\alpha$ of 1 magnitude for the emission-line nebula. This will doubtless underestimate the extinction deep inside the dusty starburst regions (e.g. nucleus A), but we are primarily interested in the energetic requirements of the large-scale nebula. The measured $H\alpha + [\text{NII}]\lambda\lambda 6548, 6584$ flux of the nebula in Armus, Heckman, & Miley (1990) then implies an extinction-corrected $H\alpha + [\text{NII}]\lambda\lambda 6548, 6584$ luminosity of $5.3 \times 10^{42} \text{ erg s}^{-1}$. Based on the typical values measured for the ratio of $[\text{NII}]\lambda 6584/H\alpha$ in the nebula (~ 0.4 to 0.5), the $H\alpha$ luminosity alone would be about $3.3 \times 10^{42} \text{ erg s}^{-1}$.

4.3. Emission Line Flux Ratios and Excitation

Emission-line flux ratios, such as $[\text{OI}]\lambda 6300/H\alpha$, $[\text{NII}]\lambda 6584/H\alpha$, $[\text{SII}]\lambda 6717 + 6731/H\alpha$ and $[\text{OIII}]\lambda 5007/H\beta$, can provide reddening-insensitive diagnostics of the ionizing sources in the Arp 299 system. The presence of the three strong “nuclear” components (A,B,

and C) along with numerous other, fainter knots which are presumably HII regions powered by young stars, are responsible for large variations of the emission-line flux ratios with position along the spectral slits in the May87 and Jan88 data. Among these data however, several trends are clear. First, the low-ionization emission line flux ratios are generally at a local minimum at the positions of the nuclei. This is most evident in the $[\text{OI}]/\text{H}\alpha$ ratio, which originates in the partially ionized region where ionized and neutral species co-exist in a bath of thermal electrons. At the position of component C, $\log [\text{OI}]/\text{H}\alpha \sim -1.8$ and $\log [\text{NII}]/\text{H}\alpha \sim -0.7$, both of which are consistent with photoionization by OB stars. Second, off the nuclei, and away from isolated HII regions, the line ratios can be much greater, reaching values of $\log [\text{OI}]/\text{H}\alpha > -1.0$ and $\log [\text{NII}]/\text{H}\alpha \sim 0$. The line ratios at various locations are summarized in Table 5.

The trends noted above can be seen more clearly if one looks at a plot of emission-line flux ratio vs. emission-line (in this case $\text{H}\alpha$) surface brightness for the off-nuclear points, as is illustrated in Fig. 13. Excluding the regions close to the nuclei, the trend of increasing $[\text{NII}]/\text{H}\alpha$ and $[\text{SII}]/\text{H}\alpha$ with decreasing nebular surface brightness is evident. In contrast the $[\text{OIII}]\lambda 5007/\text{H}\beta$ ratio is roughly constant at values of ~ 0.7 to 1.5 and shows no obvious trends with distance from the nuclei or nebular surface brightness.

In addition to the correlation of the low-ionization emission-line flux ratios with surface brightness, there is also a correlation between the emission-line flux ratios and the velocity dispersion of the gas. In Fig. 14 we plot $[\text{NII}]/\text{H}\alpha$ and $[\text{SII}]/\text{H}\alpha$ flux ratios vs. $\text{H}\alpha$ linewidth in the high resolution May87 spectra. As the line ratios increase, the velocity dispersion in the gas also increases, suggesting that the physical and dynamical states of the gas are coupled. The nuclear and near-nuclear points (those within $3''$ of the nuclei) do not obey this correlation (see Fig. 14), presumably because the line-broadening in these regions is largely gravitational in origin (e.g. we sample a significant piece of the rotation

curve within the spectroscopic sub-aperture).

In summary, the fainter, diffuse ionized gas in Arp 299 has both relatively stronger low-ionization emission lines and is more kinematically disturbed than the high-surface-brightness gas.

4.4. Gas Kinematics

With a number of slits covering the Arp 299 nebula, we can explore the gas kinematics with position, and compare these with other measurements of gas motions in the system, e.g. the HI measurements of Stanford & Wood (1989). The ionized gas kinematics can be measured via the change in emission-line centroids and widths as a function of position along the slits.

The peak velocity of the $H\alpha$ line shows variations of $100 - 300 \text{ km s}^{-1}$ across the Arp 299 nebula. In general, the velocities are blueshifted to the south and redshifted to the north, with respect to the systemic velocity of $\sim 3150 \text{ km s}^{-1}$, determined by Stanford & Wood from the centroid of the large-scale HI rotation curve. Overall, the $H\alpha$ kinematics follow the HI rotation curve. However, near the nuclei the velocity of the $H\alpha$ line is at a relative minimum, suggesting the gas in the immediate vicinity of the nuclei is blueshifted by $\sim 50 - 100 \text{ km s}^{-1}$ with respect to the systemic velocity. This might arise as consequence of a dusty outflow of gas in which the backside flow is partially obscured.

The $H\alpha$ linewidths range from less than 50 km s^{-1} to nearly 600 km s^{-1} across the Arp 299 system. As with the line centroids, spatial variations in the linewidths on the order of 200 km s^{-1} are seen on scales as small as 1.5 kpc. Near the galactic nuclei, the linewidths reach a local maximum, typically about $200 - 300 \text{ km s}^{-1}$. However, if one excludes the points near the nuclei (see above), there is a clear trend of increasing linewidth

with decreasing emission-line surface brightness, as depicted in Fig. 15. The broadest lines in the Arp 299 system, those with $\text{FWHM} > 350 - 400 \text{ km s}^{-1}$, are found in the lowest surface brightness, diffuse ionized gas in the outer regions of the nebula.

5. Discussion

5.1. The Optical Emission-Line Nebula

5.1.1. The Ionization Source

From the extinction-corrected $\text{H}\alpha + [\text{NII}]$ luminosity we estimated in §4.2 above, we deduce that the total luminosity of the optical emission-line nebula (summing over all emission lines) is $\sim 10^{44} \text{ erg s}^{-1}$. This represents about 4% of the bolometric luminosity of Arp 299 and several hundred times the X-ray luminosity of the nebula.

The luminosity of the nebula is so large that we can exclude the possibility that it is heated *primarily* by mechanical energy supplied either by the starburst or the galaxy collision itself. The rate at which a starburst produces mechanical energy (in the form of supernovae and stellar winds) is only about 1% of the starburst’s bolometric luminosity (Leitherer & Heckman 1995). Even if all this mechanical energy is used to heat the emission-line nebula, the resulting luminosity will only be 25% of the observed value. Similarly, the kinetic energy of $10^{10} M_{\odot}$ of interstellar gas moving at 300 km s^{-1} is $\sim 10^{58}$ ergs. If this energy is entirely dissipated and radiated away by the emission-line nebula during one dynamical crossing-time ($\sim 10^8$ years), the resulting heating rate is only $3 \times 10^{42} \text{ erg s}^{-1}$ or 3% of the observed value.

We conclude that the *primary* source of energy input to the optical emission-line nebula is most likely to be the ionizing radiation that escapes from the starburst complexes and

propagates into the nebula. The Leitherer & Heckman (1995) models predict a luminosity in ionizing radiation that is roughly 10% of the bolometric luminosity of the starburst, so that only about 40% of the available radiation is required to power the nebula.

This picture provides a simple and natural explanation for the inverse correlation between the relative strength of the low-ionization lines and the gas surface brightness discussed above (Fig. 13). For individual gas clouds of a given density, the higher the value of the local intensity of the ionizing radiation field, the higher the resulting value of the ionization parameter U (defined to be the ratio of the densities of ionizing photons and electrons within a photoionized gas cloud). Simple ionization equilibrium arguments show that U determines the ionization state of the gas, and the $H\alpha$ surface brightness will be proportional, through recombination, to the intensity of the ionizing radiation field. Thus, the proportionality between U and the $H\alpha$ surface brightness will naturally produce enhanced relative intensities of low-ionization lines in the faint gas (see Wang, Heckman, & Lehnert 1998).

We can examine this more quantitatively. The $H\alpha$ luminosity of the nebula (3.3×10^{42}) implies an ionization rate of $Q \sim 2.4 \times 10^{54} s^{-1}$. If we assume that this arises equally in nuclei “A” and “B1”, then the radial electron density profile discussed above (Figure 12), leads to a predicted ionization parameter $U \sim 10^{-3}$ for the gas located at radii of one to a few kpc from the nuclei. J. Sokolowski (private communication) has kindly run *CLOUDY* models of gas that is photoionized by a starburst population of hot stars using the evolutionary synthesis code discussed by Leitherer & Heckman (1995). We use the models in which the cosmically-abundant, refractory elements (e.g. Fe and Si) are locked-up in dust grains (as in the case of diffuse clouds in our own Galaxy). This depletion of gas-phase coolants has the effect of increasing the equilibrium temperature in the photoionized gas and thereby increasing the emissivity in the collisionally-excited forbidden lines with respect to the

Balmer recombination lines (Shields & Kennicutt 1995). For the above value of U , the predicted line-ratios are $[\text{SII}]\lambda\lambda\ 6716,6730/\text{H}\alpha = 0.4$, $[\text{NII}]\lambda 6583/\text{H}\alpha = 0.6$, $[\text{OI}]\lambda 6300/\text{H}\alpha = 0.03$, and $[\text{OIII}]\lambda 5007/\text{H}\beta = 1.6$, in reasonable agreement with the typical observed values in the *high*-surface-brightness part of the nebula (Figures 11, 13, and 14; Table 5).

While photoionization clearly dominates the total energy input into the nebula and the excitation near the nuclei, mechanical heating also plays an important role, especially in the diffuse low-surface-brightness gas. Firstly, recall that the estimated mechanical luminosity of the starburst is 25% of the nebula’s emission-line luminosity. Secondly, the good correlation we find between the widths of the emission-lines and the line-ratios (Figure 14) suggests that there is a connection between the dynamics of the gas and its physical state (as expected for shock heating). Finally, shock-heating may be required to explain the extreme line-ratios present in the very faint outer regions where $[\text{OI}]/\text{H}\alpha = 10$ to 20% and $[\text{OIII}]/\text{H}\beta \sim 1$ (see Table 5). Most likely, both photoionization and shocks play a role, with the former being more globally significant, and the latter being important in the most kinematically-disturbed (faint, outer) regions.

5.1.2. *The Pressure Profile*

One property of the emission-line nebula that can be most clearly ascribed to the mechanical energy supplied by the starburst is the gas density/pressure profile (Figure 12). In the starburst-driven wind models of Chevalier & Clegg (1985), there is a region of radius r_* (the starburst) inside which mass and kinetic energy are injected at a constant rate per unit volume, resulting in a region of hot gas which slowly expands through a sonic radius (located approximately at the radius of the starburst) and is then transformed into a supersonic outflow.

The gas pressure inside the starburst is just the static, thermal pressure of the hot fluid that has been produced by thermalization (shock-heating) in high-speed collisions between material ejected by supernovae and the ambient interstellar medium. This pressure is essentially determined by the size of the starburst and the rate at which mass and kinetic energy is injected. Since the sound-crossing time inside the starburst is much shorter than the outflow time (e.g. since the flow is subsonic inside the starburst itself), the pressure is roughly constant throughout this central region.

Using the starburst models of Leitherer & Heckman (1995) to relate the rate at which the starburst injects mass and thermal/mechanical energy to its bolometric luminosity, we expect the central pressure to be given approximately by:

$$P_0/k = 3 \times 10^6 L_{bol,11} [r_*/kpc]^{-2} \text{ K cm}^{-3} \quad (1)$$

At radii much larger than the starburst radius, the pressure of the outflow is dominated by the wind's ram pressure. This will essentially be set by the rate at which the starburst injects mass and energy into the outflow, and will drop like the inverse square of distance from the starburst:

$$P(r)/k = 3 \times 10^6 L_{bol,11} [r/kpc]^{-2} \text{ K cm}^{-3} \quad (2)$$

where r is the distance from the starburst (assuming $r \gg r_*$).

These predictions agree reasonably well with the observations of Arp 299. Taking $L_{bol} = 3 \times 10^{11} L_{\odot}$ as a rough estimate of bolometric luminosity for each of the two starbursts and $r_* = 1.3$ kpc as their estimated radii, the predicted value $P/k = 5 \times 10^6 \text{ K cm}^{-3}$ is the same as that derived from the temperatures and densities given in §4.1. Similarly, the predicted value for P/k at a radius of 3 kpc is $\sim 10^6 \text{ K cm}^{-3}$ ($n_e = 50 \text{ cm}^{-3}$), consistent

with Figure 12.

5.2. The X-Ray Nebula

In principle, the X-ray nebula could arise as a significant fraction of the gas initially in the disks of two spiral galaxies is heated collisionally during the galaxies’ on-going merger. As discussed in §5.1 above, the maximum rate of collisional heating in a merger will be of-order $3 \times 10^{42} \text{ erg s}^{-1}$, which is about an order-of-magnitude larger than the observed X-ray luminosity. The mass of hot gas ($7 \times 10^9 M_{\odot}$) is also consistent with this picture.

There are however at least two problems with this model. First, the observed gas temperatures are much too high in the inner region. That is, cloud collision speeds appropriate to a galactic merger (300 to 500 km s⁻¹) correspond to postshock temperatures of 1.3 to 3.5 million K, while the observed temperature is 9 million K in the inner region. Second, if X-ray nebulae in colliding/merging galaxies are directly produced by the galactic collision, then we would expect that bright X-ray nebulae would be a common feature of mergers of disk galaxies (regardless of whether these mergers are undergoing a starburst). Wang et al (1997) and Read & Ponman (1998) have shown that this is *not* the case. In the Wang et al sample of 12 merging/colliding galaxies (including Arp 299), the only strong soft X-ray emitters are also strong H α + [NII] and far-IR emitters. Put another way, strong soft X-ray emission is not a ubiquitous feature of galaxy mergers (Read & Ponman 1998), but instead appears to share a common power source with the optical line and far-IR emission (a starburst). We therefore regard the most likely origin of the X-ray nebula in Arp 299 to be a superwind.

Evidence for outflowing gas in Arp 299 comes from the optical spectroscopic data on the kinematically-disturbed faint emission-line filaments and loops (see §4.4). The presence

of diffuse X-ray-emitting gas extending well outside the optical boundaries of the galaxy and oriented roughly perpendicular to the system's HI major axis is also highly suggestive of an outflow. In order to quantitatively assess whether the soft X-ray emission can indeed be produced by gas heated by supernovae and stellar winds in the central star-bursting complexes, we will adopt a simple model that assumes that mechanical energy is being continuously injected inside the starburst and used to heat the surrounding gas. This gas then flows out of the starburst and emits X-rays (cf. Wang 1995). In such a model we need to specify the heating rate and the mass-injection rate into the outflow.

As noted earlier, the IR luminosity of Arp 299, when used in conjunction with the starburst models of Leitherer & Heckman (1995), corresponds to a total mechanical heating rate of about $2 \times 10^{43} \text{ erg s}^{-1}$. We will assume that the gas in the starburst is initially heated to a temperature of about $9 \times 10^6 \text{ K}$ (the temperature of the hottest diffuse gas that we detect in our X-ray data). For the heating rate given above, conservation of energy then implies that gas is heated at a rate of $\sim 100 \text{ M}_{\odot}$ per year (Chevalier & Clegg 1985). This is about an order of magnitude greater than the predicted rate at which supernovae and stellar winds return mass to the interstellar medium in this system. This implies that the outflow is strongly "mass-loaded": most of the outflowing material is ambient interstellar gas in and around the starburst that has been heated by the supernovae and stellar winds (see Suchkov et al 1996). In effect, each supernova heats up, on average, about 200 M_{\odot} of interstellar gas. In this case, we would expect the average metallicity of the X-ray emitting gas to be similar to that in the interstellar medium of Arp 299.

Since the predicted mechanical heating rate is about 10^2 times the total luminosity of the two MEKAL thermal components, we will ignore the dynamical effect of radiative cooling in our simple model. This neglect is further justified since the estimated radiative cooling time of the X-ray gas (approximately a Gyr - see §3.3 above) is much longer than

the adiabatic expansion timescale ($\sim \text{few} \times 10^7$ years).

Following Chevalier & Clegg (1985) and Wang (1995) we therefore consider a spherically-symmetric wind with a mass outflow rate of $100 M_\odot$ per year which is “fed” by hot gas that is injected at a uniform temperature of 9×10^6 K. We will take the overall size of the energy injection region (encompassing both the Eastern and Western starbursts) to be similar to that of the bright X-ray emission in the HRI data (radius ~ 4 kpc). This is obviously an oversimplification, but might roughly represent the effect of the collision between the two outflows produced by the Eastern and Western starbursts, and the subsequent shocks and rethermalization of the gas on these size-scales. In the absence of gravitational deceleration, the wind would reach a terminal velocity of $v_{\text{wind}} = 800 \text{ km s}^{-1}$ (Chevalier & Clegg 1985). We assume the wind cools through adiabatic expansion while also emitting soft X-rays. The emissivity of gas in the 0.1 to 2.4 keV energy band is constant to within about a factor of ~ 3 as a function of temperature over the range between 4×10^5 K to 5×10^7 K ($\simeq 2 \times 10^{-23} \text{ erg cm}^3 \text{ s}^{-1}$ for solar metallicity). This then allows us to predict an X-ray luminosity from the outflow of $\simeq 4 \times 10^{41} \text{ erg s}^{-1}$ from within a region equal in size to the X-ray halo (radius of ~ 20 kpc). This rough estimate compares reasonably well with the measured luminosity of the two MEKAL X-ray components of $2 \times 10^{41} \text{ erg s}^{-1}$. The total predicted mass of the hot gas will be about $3 \times 10^9 M_\odot$ and the predicted thermal plus kinetic energy in the outflow will be $2 \times 10^{58} \text{ ergs}$. Again, these predicted values agree reasonably well with the derived values for the sum of the hot (0.77 keV) and warm (0.2 keV) components: $M \simeq 7 \times 10^9 f^{1/2} M_\odot$ and $E_{\text{therm}} \simeq 10^{58} f^{1/2} \text{ ergs}$.

Note that a radius of 20 kpc and a wind terminal velocity of 800 km s^{-1} corresponds to a rough dynamical age of 25 Myr (reasonable for a starburst). If the outflow has lasted much longer than this, the total mass and energy in the flow will rise accordingly, but this will comprise material at larger radii (> 20 kpc). Such material will have a low density and

(due to adiabatic cooling) a low temperature, and would therefore not produce significant X-ray emission (cf. Wang 1995). In fact, our simple model predicts a temperature range in the hot gas ranging from 9×10^6 K in the energy injection region to 6×10^6 K at a radius of 4 kpc to 5×10^5 K at a radius of 20 kpc. These temperatures then span the observed/inferred range, and the temperatures reach the lower limit where the ROSAT PSPC sensitivity plummets ($T \leq 4 \times 10^5$ K) at roughly the same radius as where the observed emission ends.

Having demonstrated that this simple model can very roughly reproduce the gross properties of the X-ray emission, we next consider the fate of this outflowing gas. Following Wang (1995), the “escape temperature” for hot gas in a galaxy potential with an escape velocity v_{es} is given by:

$$T_{es} \simeq 9.9 \times 10^5 (v_{es}/300 \text{ km s}^{-1})^2 \text{ } ^\circ\text{K}$$

The HI rotation curve of Arp 299 has an amplitude of 240 km s^{-1} out to the edge of the HI distribution at a radius of 22 kpc (Stanford & Wood 1989). Assuming that Arp 299 has an isothermal dark matter halo extending to a radius of 300 kpc, the escape velocity (see equation 13 in Heckman et al. (1995)) at $r = 4$ (22) kpc is about 780 (650) km s^{-1} and $T_{es} = 6.7$ (4.6) $\times 10^6$ K. These temperatures are similar to the range of temperatures we measure for the hot gas ($\simeq 2 \times 10^6$ K for the cooler component and $\simeq 9 \times 10^6$ K for the hotter component). The escape velocity is also similar to the estimated terminal velocity for the wind (see above). These rough arguments suggest that the outflowing gas *may* be able to escape the gravitational potential of Arp 299.

6. Conclusions

We have discussed optical and X-ray data on the spectacular gaseous nebula surrounding the infrared-luminous merger/starburst system Arp 299 (= NGC 3690 or Mrk 171).

We suggest that the on-going galaxy collision has tidally redistributed the cold interstellar media of the merging galaxies. The total luminosity of the optical emission-line nebula (10^{44} erg s $^{-1}$ \sim 4% L_{bol}) is too high to be powered primarily by either the collision of two galaxies directly, or by a starburst-driven superwind. Instead, the gas is mostly photoionized by radiation from the ongoing starburst.

We find strong trends in which the relative strengths of low-ionization lines ([SII], [NII], and [OI]) increase systematically with both decreasing nebular surface brightness and with increasing velocity dispersion. These trends can be understood if both hot stars and large-scale shocks play a role in energizing the gas. The shocks become increasingly important in the faint, outer regions of the nebula, and they provide for the coupling between the dynamical and physical state of the gas.

We also find that the gas pressures are high in the inner optical emission-line nebula ($P/k \sim 5 \times 10^6$ K cm $^{-3}$ within a radius of a kpc, and fall systematically with radius (dropping below $P/k \sim 10^6$ K cm $^{-3}$ at a radius of ~ 3 kpc). The shape and amplitude of the radial pressure profile agrees with the pressures predicted for starburst-driven outflows.

While the luminosity ($\sim 2 \times 10^{41}$ erg s $^{-1}$) and mass ($\sim 7 \times 10^9$ M $_{\odot}$) of the X-ray nebula can be explained by the collision of the interstellar media of two galaxies, we believe a more plausible heating source is the superwind. The thermal energy content ($\sim 10^{58}$ ergs) and dynamical age ($\sim few \times 10^7$ years) of the X-ray nebula agree with a superwind model, but its high gas mass and X-ray luminosity, and its relatively low temperature (9 million K in

the inner region and 2.3 million K in the outer) imply that the outflow must be strongly ‘mass-loaded’ (most of the X-ray emitting gas is ambient interstellar material that has been mixed into the outflow). The implied outflow rate of $\sim 100 M_{\odot}$ per year can be compared to the estimated star-formation rate in the starburst of 40 (100) M_{\odot} per year for a Salpeter IMF extending down to 1 (0.1) M_{\odot} . The inner gas temperature of 9 million K implies a terminal velocity for such a flow of about 800 km s^{-1} . These respective values are similar to the estimated escape temperature and escape velocity from the system.

Thus, perhaps the most striking result of this investigation is that in Arp 299 a powerful starburst has apparently been able to heat up a significant fraction of the interstellar medium of the merger product (nearly $10^{10} M_{\odot}$) to a temperature and outflow speed that may allow this gas ultimately to escape the system. This has implications for understanding how disk-disk galaxy mergers may produce (at least some) elliptical galaxies (Mihos & Hernquist 1994; Schweizer 1992) and how the intergalactic medium could have been polluted by metal-enriched material (see Gibson, Loewenstein, & Mushotzky 1997).

REFERENCES

- Aalto, S., Radford, S., Simon, J., Scoville, N., & Sargent, A. 1997, *ApJL*, 475, L107
- Armus, L., Heckman, T., & Miley, G. 1989, *ApJ*, 347, 727
- Armus, L., Heckman, T., & Miley, G. 1990, *ApJ*, 364, 471
- Baan, W., & Haschick, A. 1990, 364, 65
- Beck, S., Turner, J., & Ho, P. 1986, *ApJ*, 309, 70
- Blain, A., Smail, I., Ivison, R., & Kneib, J.-P. 1998, *MNRAS*, in press
- Bland-Hawthorn, J. 1995, *PASA*, 12, 190
- Bregman, J., & Pildis, R. 1992, *ApJL*, 398, L107
- Burstein, D., & Heiles, C. 1982, *AJ*, 87, 1165
- Cash, W. 1979, *ApJ*, 228, 939
- Chevalier, R. & Clegg, A. 1985, *Nature*, 317, 44
- Collura, A., Reale, F., Schulman, E., & Bregman, J. 1994, *ApJL*, 418, L67
- Condon, J.J. 1991, *ApJ*, 378, 65
- Condon, J.J., Helou, G., Sanders, D., & Soifer, B.T. 1990, *ApJS*, 73, 359
- Dahlem, M., Heckman, T., & Fabbiano, G. 1995, *ApJL*, 442, L49
- Dahlem, M., Weaver, K., and Heckman, T. 1998, *ApJS*, in press
- David, L. et al. 1997, The *ROSAT* HRI Calibration Report, <http://he-www.harvard.edu/rosat/rsdc/www/HRI-CAL-REPORT/>

- Dopita, M. & Sutherland, R. 1996, *ApJS*, 102, 161
- Fischer, J., Simon, M., Benson, J., & Solomon, P. 1983, *ApJL*, 273, L27
- Gerhaz, R., Sramek, R., & Weedman, D. 1983, *ApJ*, 267, 551
- Genzel, R., Lutz, D., Sturm, E., Egami, E., Kunze, D., Moorwood, A., Rigopoulou, D., Spoon, H., Sternberg, A., Tacconi-Garman, L., Tacconi, L., & Thatte, N., 1998, *ApJ*, 498, 579
- Gibson, B., Loewenstein, M., & Mushotzky, R. 1997, *MNRAS*, 290, 623
- Harwit, M., Houck, J., Soifer, B.T., & Palumbo, G. 1987, *ApJ*, 315, 28
- Heckman, T. 1998, in *ORIGINS*, ASP Conf. Series, Vol. 148, Ed. C.E. Woodward, J.M. Shull, and H.A. Thronson, Jr,
- Heckman, T.M., Armus, L. and Miley, G.K. 1990, *ApJS*, 74, 833
- Heckman, T., Lehnert, M., & Armus 1993, in *The Evolution of Galaxies and their Environments*, Ed. J.M. Shull and H. Thronson, Jr, Kluwer, 455
- Heckman, T., Dahlem, M., Lehnert, M., Fabbiano, G., Gilmore, D., & Waller, W. 1995, *ApJ*, 448, 98
- Heckman, T., Dahlem, M., Eales, S., Fabbiano, G., & Weaver, K. 1996, *ApJ*, 457, 616
- Hibbard, J. 1997, in *Star-Formation Near and Far*, Ed. S. Holt and L. Mundy (AIP: Woodbury, NY), p. 259
- Hughes, D., Serjeant, S., Dunlop, J., Rowan-Robinson, M., Blain, A., Mann, R., Ivison, R., Peacock, J., Efstathiou, A., Gear, W., Oliver, S., Lawrence, A., Longair, M., Goldschmidt, & Jenness, T. 1998, *Nature*, in press

Iwasawa, K., & Comastri A., 1998, MNRAS, in press

Joy, M., Lester, D., Harvey, P., Telesco, C., Decher, R., Rickard, L., & Bushouse, H. 1989, ApJ, 339, 100

Kaastra, J.S. 1992, An X-Ray Spectral Code for Optically Thin Plasmas (Internal SRON-Leiden Report, updated version 2.0)

Kohmura, Y. et al. 1994, PASJ, 46, L157

Leitherer, C., & Heckman, T. 1995, ApJS, 96, 9

Marlowe, A., Heckman, T., Wyse, R., & Schommer, R. 1995, ApJ, 438, 563

Mathis, J. 1990, ARA&A, 28, 37

Meurer, G., Heckman, T., Leitherer, C., Kinney, A., Robert, C., & Garnett, D. 1995, AJ, 110, 2665

Meurer, G., Heckman, T., & Calzetti, D. 1998, submitted to ApJ

Mewe, R., Gronenschild, E.H.B.M., & van den Oord, G.H.J. 1985, A&AS, 62, 197

Mewe, R., Lemen, J.R., & van den Oord, G.H.J. 1986, A&AS, 65, 511

Mihos, J.C., & Hernquist, L. 1994, ApJ, 431, L9

Moran, E., & Lehnert, M. 1997, ApJ, 478, 172

Nakagawa, T., Nagata, T., Geballe, T., Okuda, M., Shibai, H., & Matsuhara, H. 1989, ApJ, 340, 729

Read, A. & Ponman, T. 1998, MNRAS, in press

- Ryder, S., Staveley-Smith, L., Dopita, M., Petre, R., Colbert, E., Malin, D., & Schlegel, E. 1993, *ApJ*, 416, 167
- Sanders, D., & Mirabel, I.F. 1997, *ARAA*, 34, 749
- Sargent, A., & Scoville, N. 1991, *ApJL*, 366, L1
- Schweizer, F. 1992, in *Physics of Nearby Galaxies: Nature or Nature?*, Ed. T. Thuan et al., Editions Frontieres: Gif-sur-Yvette, 283
- Seaquist, E. R. & Odegard, N. 1991, *ApJ*, 369, 320
- Shields, J.C. and Kennicutt, Jr. R.C. 1995, *ApJ*, 454, 807
- Soifer, B.T., Sanders, D., Madore, B., Neugebauer, G., Lonsdale, C., Persson, S.E., & Rice, W. 1987, *ApJ*, 320, 238
- Stanford, S.A., and Wood, D.O.S. 1989, *ApJ*, 346, 712
- Steidel, C., Giavalisco, M., Pettini, M., Dickinson, M., & Adelberger, K. 1996, *ApJ*, 462, L17
- Suchkov, A. Berman, V., Heckman, T., & Balsara, D. 1996, *ApJ*, 463, 528
- Sutherland & Dopita 1993, *ApJS*, 88, 253
- Tanaka, Y., Inoue, H., & Holt, S. S. 1994, *PASJ*, 46, L137
- Telesco, C., Decher, R., & Gatley, I. 1985, *ApJ*, 299, 896
- Veilleux, S., Kim, D.-C., Sanders, D., Mazzarella, J., & Soifer, B.T. 1995, *ApJS*, 98, 171
- Wang, B. 1995, *ApJ*, 444, 590
- Wang, J., Heckman, T., Weaver, K., & Armus, L. 1997, *ApJ*, 474, 659

Wang, J., Heckman, T., & Lehnert, M. 1998, ApJ, in press

Weaver, K., Heckman, T., & Dahlem, M. 1998, in preparation

Wynn-Williams, G., Eales, S., Becklin, E., Hodapp, K., Joseph, R., McLean, I., Simons, D.,
& Wright, G. 1991, ApJ, 377, 426

Zezas, A., Georgantopoulos, I., & Ward, M. 1998 (ZGW), MNRAS, in press

Zimmermann, H.-U. et al. 1994, Nature, 367, 621

Table 1: Spatially-Resolved PSPC Spectra

Region	Geom.	Extent		Orientation	Area	Rate	Counts ^b
	Shape	Maj. ax. a [']	Min. ax. b [']	PA [°]	[arcmin ²]	[c/s]	
Total	Ellipse	2.78	2.22	193	19.38	0.099	983
Core	Circle	1.3	1.3		5.31	0.087	863
Halo	Ellipse – Circle				14.07	0.012	119

Notes to Table 1:

^aRegions used to extract the PSPC spectra discussed in §3.2. The halo region is bounded by the elliptical region used to extract the total spectrum and the circular region used to extract the core spectrum.

^bTotal number of source counts.

Table 2: Results of PSPC Spectral Modelling

Region ^a	Model ^b	N_H^c	kT_M^d	Z^e/Z_\odot	Γ or (kT_B^f)	$(\chi^2/\nu)^g$
H	B	0.9(f)	$0.20^{+0.12}_{-0.07}$	1.0
C	A	$7.4^{+2.6}_{-1.6}$	2.4 ± 0.3	83/33
C	B1	0.9(f)	$0.83^{+0.10}_{-0.04}$	1.0	...	66/34
C	B2	$1.2^{+0.6}_{-0.4}$	$0.83^{+0.16}_{-0.09}$	1.0	...	63/33
C	B3	$4.0^{+1.6}_{-1.4}$	$0.85^{+0.15}_{-0.13}$	$0.12^{+0.28}_{-0.07}$...	41/32
C	C	$2.2^{+0.9}_{-0.6}$	$0.70^{+0.14}_{-0.18}$	1.0	7.0(f)	29/32

Notes to Table 2:

^aThe spectral extraction region; H=halo and C=core; f=fixed parameter.

^bModels are A: absorbed power-law, B: MEKAL plasma with absorption ($N_H(\text{Gal}) = 0.9 \times 10^{20} \text{ cm}^{-2}$), C: MEKAL plasma and thermal Bremsstrahlung with absorption.

^cThe absorbing column density in units of 10^{20} cm^{-2} .

^dThe MEKAL temperature in units of keV.

^eMEKAL plasma abundance in solar units.

^fThe photon index (or temperature) of the hard X-ray power law (or Bremsstrahlung component in units of keV.)

^gValue of χ^2 divided by the number of degrees of freedom.

Errors are $\chi^2_{\min} + 4.61$ or 6.25, which are 90% confidence for 2 or 3 free parameters.

Table 3: Results of joint PSPC and ASCA fits

Model ^a	kT_{M2}^b [keV]	Z/Z_{\odot}^c	A_{M2}^d [10^{-3}]	N_H^e [10^{20}]	Γ^f or (kT_B^f)	A_H^g [10^{-4}]	χ^2/ν^h (χ^2_{nu})
A	5.6 ± 1.0	2.27 ± 0.11	4.3 ± 0.2	439/279 (1.57)
B	$2.7^{+0.4}_{-0.3}$	$0.07^{+0.13}_{-0.07}$	1.4 ± 0.2	2.8 ± 0.5	537/278 (1.93)
C	$0.70^{+0.12}_{-0.07}$	$0.27^{+0.38}_{-0.21}$	$0.68^{+0.74}_{-0.58}$	2.6 ± 0.7	$1.51^{+0.22}_{-0.27}$	$1.6^{+0.4}_{-0.6}$	285/276 (1.03)
D1 ⁱ	$0.77^{+0.08}_{-0.17}$	1.0(f)	$0.18^{+0.02}_{-0.04}$	$7.2^{+6.7}_{-4.0}$	$1.6^{+0.15}_{-0.20}/(11^{+10}_{-4})$	$2.1^{+0.2}_{-0.3}/(2.4)$	279/276 (1.01)
D2 ⁱ	$0.77^{+0.08}_{-0.17}$	1.0(f)	$0.14^{+0.02}_{-0.03}$	$6.2^{+6.0}_{-3.7}$	$1.6^{+0.15}_{-0.20}/(11^{+10}_{-4})$	$2.2^{+0.2}_{-0.3}/(2.5)$	281/276 (1.02)

Notes to Table 3:

^aModels are A: absorbed power law, B: MEKAL with absorption; C:MEKAL plus power law with absorption, and D: 2-temperature MEKAL plus hard component.

^bMEKAL temperature.

^cPlasma abundance.

^dMEKAL normalization in units of $10^{-14}/(4\pi D^2) \int n_e n_H dV$, where D is the distance to the source (cm), and n_e and n_H are the electron and hydrogen densities (cm^{-3})

^eAbsorbing column density in units of cm^{-2} .

^fThe photon index (or Bremsstrahlung temperature in units of keV).

^gNormalization of the hard component. The power-law normalization is in units of photons $\text{keV}^{-1} \text{cm}^{-2} \text{s}^{-1}$ at 1 keV; the bremsstrahlung normalization is in units of $3.02 \times 10^{-15}/(4\pi D^2) \int n_e n_i dV$, where n_e is the electron density (cm^{-3}), n_i is the ion density (cm^{-3}), and D is the distance to the source (cm).

^hValue for χ^2 divided by the number of degrees of freedom (reduced χ^2).

ⁱThe soft component (not listed) has $kT = 0.2 \text{ keV}$ and $N_H = 0.9 \times 10^{20} \text{ cm}^{-2}$. For model D1, the intrinsic absorption (column 5) is applied to the medium and hard components. For model D2, the intrinsic absorption is only applied to the hard component. The MEKAL normalization of the soft component is $0.84^{+0.32}_{-0.31}$ (D1) and $0.51^{+0.21}_{-0.20}$ (D2); same units as column 4.

Table 4: Absorption-corrected Fluxes from the *ROSAT* PSPC and *ASCA* fits

Model	$F_{(0.1-2.4)\text{M1}}^a$	$F_{(0.1-2.4)\text{M2}}^b$	$F_{(2-10)\text{M2}}^c$	$F_{(2-10)\text{Hard}}^d$	$F_{(0.1-2.4)\text{Hard}}^e$
C	...	7.0 ± 0.4	0.18 ± 0.03	11.0 ± 0.2	9.0 ± 0.4
D1	2.3 ± 0.6	5.6 ± 0.8	0.23 ± 0.09	10.0 ± 0.2	6.6 ± 0.3
D2	1.4 ± 0.5	4.5 ± 0.6	0.18 ± 0.08	10.7 ± 0.3	6.6 ± 0.3

Notes to Table 4:

Fluxes are given in units of 10^{-13} ergs cm^{-2} s^{-1} . The models in column 1 correspond to those described in Table 3.

^aThe 0.1 – 2.4 keV flux for the 0.2 keV MEKAL component, derived from the PSPC.

^bThe 0.1 – 2.4 keV flux for the ~ 0.75 keV MEKAL component, derived from the PSPC.

^cThe 2 – 10 keV flux for the ~ 0.75 keV MEKAL component, derived from *ASCA*. *ASCA* fluxes are instrument-averaged fluxes.

^dThe 2 – 10 keV flux for the hard X-ray component, derived from *ASCA*.

^eThe 0.1 – 2.4 keV flux for the hard X-ray component, derived from *ASCA*.

Table 5: Optical Emission-Line Ratios in Arp 299

Location	Log of Line Ratio				
	$[\text{OIII}]\lambda 5007/\text{H}\beta$	$\text{H}\alpha/\text{H}\beta$	$[\text{OI}]\lambda 6300/\text{H}\alpha$	$[\text{NII}]\lambda 6584/\text{H}\alpha$	$[\text{SII}]\lambda 6724/\text{H}\alpha$
A	−0.05	0.80	−1.08	−0.34	−0.37
B	−1.24	−0.34	−0.50
C	0.00	0.53	−1.75	−0.47	−0.72
HSB NEB	−0.1	0.57	−1.6	−0.6	−0.6
	0.0	0.80	−1.0	−0.3	−0.3
LSB NEB	−0.1	0.46	−1.3	−0.6	−0.5
	0.1	0.60	−0.6	−0.2	−0.1

Notes to Table 5:

We adopt the nomenclature of Gehrz, Sramek, & Weedman (1983) wherein source A corresponds to the nucleus of the Eastern galaxy, source B corresponds to the nucleus of Western galaxy, and source C is another site of intense activity in this galaxy. These values are taken from Armus, Heckman, & Miley (1989).

We divide the off-nuclear regions of the Arp 299 into regions of high- and low- $\text{H}\alpha$ surface-brightness, since the properties of the emission-line gas correlate well with this parameter (see Figures 13 and 15 and text for details). For both regions we list the range of typical values for these line ratios, from minimum (top line) to maximum (bottom line). See Figure 13 and the text.

Fig. 1.— *ROSAT* PSPC 0.1 – 2.4 keV image of Arp 299 superimposed on the digital sky-survey optical image. The X-ray data have been blocked by a factor of three, and then smoothed with a Gaussian kernel having a $\sigma = 5$ pixels (7.5").

Fig. 2.— *ROSAT* PSPC (a) hard-band and (b) soft-band contours for Arp 299. The X-ray images cover the energy bands of 0.1 – 0.5 and 0.5 – 2.4 keV, respectively. The data have been blocked by a factor of three (as in Fig. 1) and then smoothed with a Gaussian kernel having a $\sigma = 10$ pixels (15 arcseconds). The contours in Fig. 2a are drawn at 90, 75, 50, 25, 10, 5, and 3% of the peak value. The contours in Fig. 2b are drawn at 90, 70, 60, 50, and 30% of the peak value. The lowest contour is at the $\sim 5\sigma$ level.

Fig. 3.— Two views of the *ROSAT* HRI image overlaid on the continuum subtracted $H\alpha + [NII]$ image from Armus, Heckman & Miley (1990). In both frames the HRI data, shown as contours, have been blocked into 2" pixels and then smoothed with a Gaussian having a $\sigma = 1.5$ pixels ($\sim 7''$ FWHM). North is up and east is to the left in both frames. The position of nucleus "A" is indicated by a cross in the upper frame.

Fig. 4.— *ROSAT* PSPC spatially-resolved spectra of the core and halo regions shown together for comparison. The sizes of the extraction regions are listed in Table 1. Triangles indicate the halo spectrum; crosses indicate the core spectrum.

Fig. 5.— Ratio of the *ROSAT* PSPC spectrum of the core region in Arp 299 to models consisting of (a) a power law (chosen to illustrate the line emission near 0.9 keV), (b) a MEKAL plasma with free N_H and solar abundances (Model B2 in Table 2), (c) a MEKAL plasma plus thermal bremsstrahlung with free N_H and solar abundances (Model D in Table 2).

Fig. 6.— Ratio of the *ROSAT* PSPC and *ASCA* data to a MEKAL plasma model with free abundances (model B in Table 3).

Fig. 7.— *ROSAT* PSPC and *ASCA* data and the best-fitting three-component model folded through the instrumental response (model D2 in Table 3). Data from all detectors are shown.

Fig. 8.— The three-component model that best describes the $\sim 0.1 - 10$ keV X-ray spectrum of Arp 299. Here, extra N_H is applied to both the medium and hard components (Model D2).

Fig. 9.— The ratio of the *ROSAT* PSPC and *ASCA* data to the best-fitting three-component model (model D2 in Table 3).

Fig. 10.— Continuum subtracted $H\alpha + [NII]$ image of Arp 299 showing the positions of the spectroscopic slits discussed in the text. The slits used to obtain the medium resolution May87 data are indicated by solid lines, while the slits used to obtain the low resolution Jan88 data are indicated by dashed lines.

Fig. 11.— Medium resolution spectra extracted from the May87 longslit data at various positions throughout the Arp 299 nebula. Spectra of components “B1” and “C”, are shown in Figs. 11a & 11b, respectively. Fig. 11c is from a position, $2''$ north of component “A”. Figs. 11a-c have been created by summing $4.5''$ along the slit. The spectrum of the gas directly between components “A” and “C” is shown in Fig. 11d, created by summing $10''$ along the slit, centered $11''$ east of component “C”. Figs. 11e-g are spectra extracted from the faint, nebular gas as follows: (11e) $24''$ west of “C”, summed over $32''$; (11f) $23''$ west of “B1”, summed over $13''$; (11g) $24''$ north and $6.5''$ east of “A”, summed over $23''$. In all cases, a relative flux density scale is plotted on the y-axis and wavelength, in \AA is plotted along the x-axis. See Fig. 10 for a visual representation of the slits on the $H\alpha + [NII]$ image of Arp 299.

Fig. 12.— Plot of the log of electron density (cm^{-3}), as measured from the ratio of the [SII] lines in the May87 data, as a function of log of the distance (kpc) from the Arp 299 nuclei. For the western part of the nebula the distance was measured with respect to the centroid of sources B and C, while in the eastern part the distances are measured with respect to source A. See text for details. The shape and normalization of the radial density profile (and hence the pressure profile) is as expected in the superwind model.

Fig. 13.— Plot of emission-line flux ratio vs. $\text{H}\alpha$ surface brightness (in arbitrary units) of the emission-line gas in the Arp 299 nebula. Squares refer to the ratio of $[\text{NII}]\lambda 6584/\text{H}\alpha$ and triangles refer to $[\text{SII}]\lambda\lambda 6717,6731/\text{H}\alpha$. The open (solid) symbols refer to gas located at radii $\leq (>)$ 3 arcsec from the galaxy nuclei. Notice the trend of increasing $[\text{NII}]/\text{H}\alpha$ and $[\text{SII}]/\text{H}\alpha$ with decreasing surface brightness for the off-nuclear regions (solid symbols).

Fig. 14.— The $[\text{NII}]/\text{H}\alpha$ (squares) and $[\text{SII}]/\text{H}\alpha$ (triangles) flux ratios vs. the FWHM of the the $\text{H}\alpha$ line (km s^{-1}). The open (solid) symbols refer to gas located at radii $\leq (>)$ 3 arcsec from the galaxy nuclei. Notice the trend of increasing line-flux ratio with increasing $\text{H}\alpha$ line width in the off-nuclear gas (solid symbols), consistent with the idea of shocks exciting the faintest extra-nuclear gas and disturbing it kinematically.

Fig. 15.— Plot of the $\text{H}\alpha$ surface brightness (arbitrary units) versus the the $\text{H}\alpha$ linewidth (FWHM in km s^{-1}). The open (solid) symbols refer to gas located at radii $\leq (>)$ 3 arcsec from the galaxy nuclei. The correlation of increasing linewidth and decreasing nebular surface brightness is clear in the off-nuclear region (solid symbols).

Arp 299

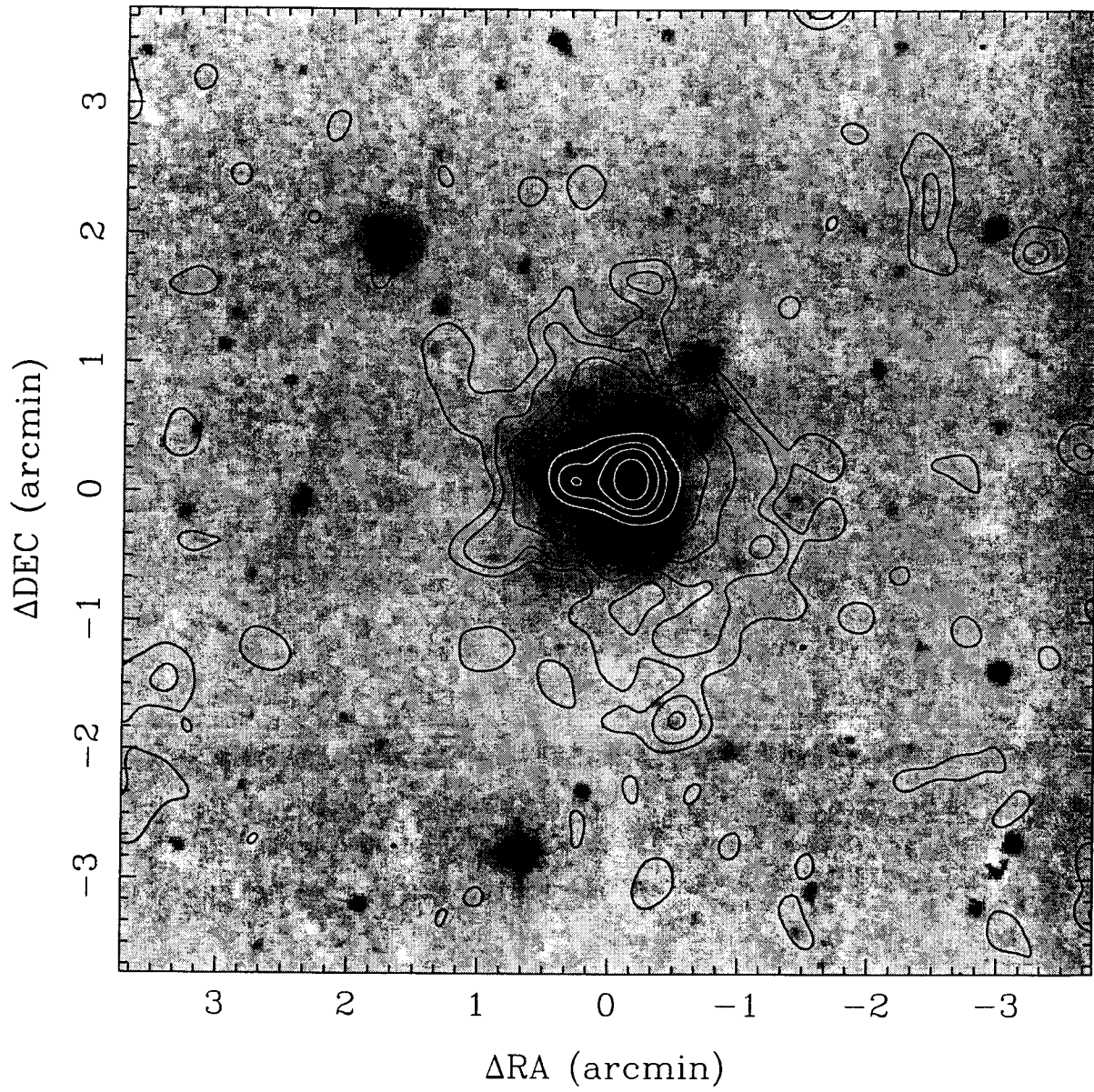


Fig. 1

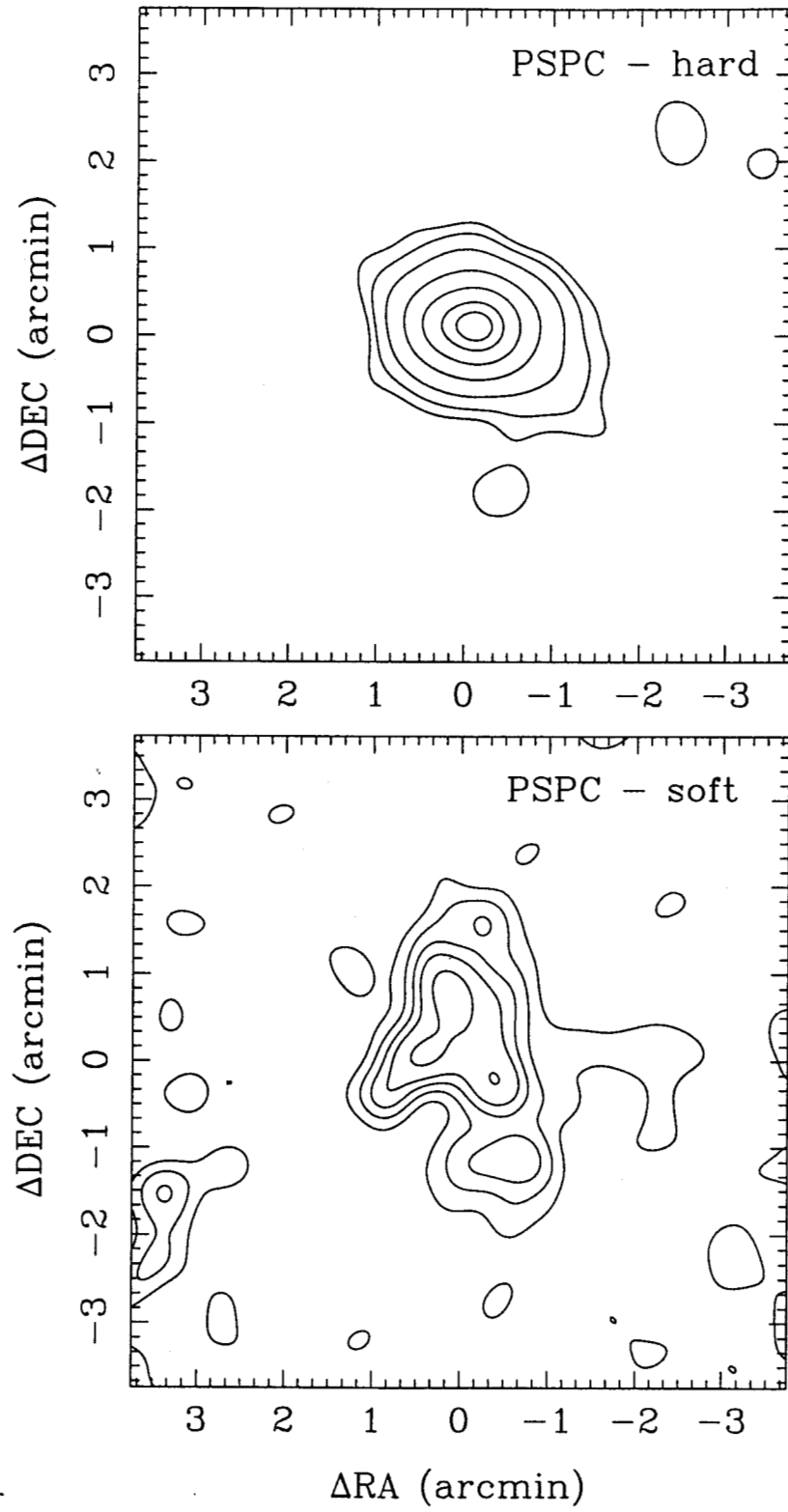


Fig. 2

Arp 299 - HRI & H α + [NII]

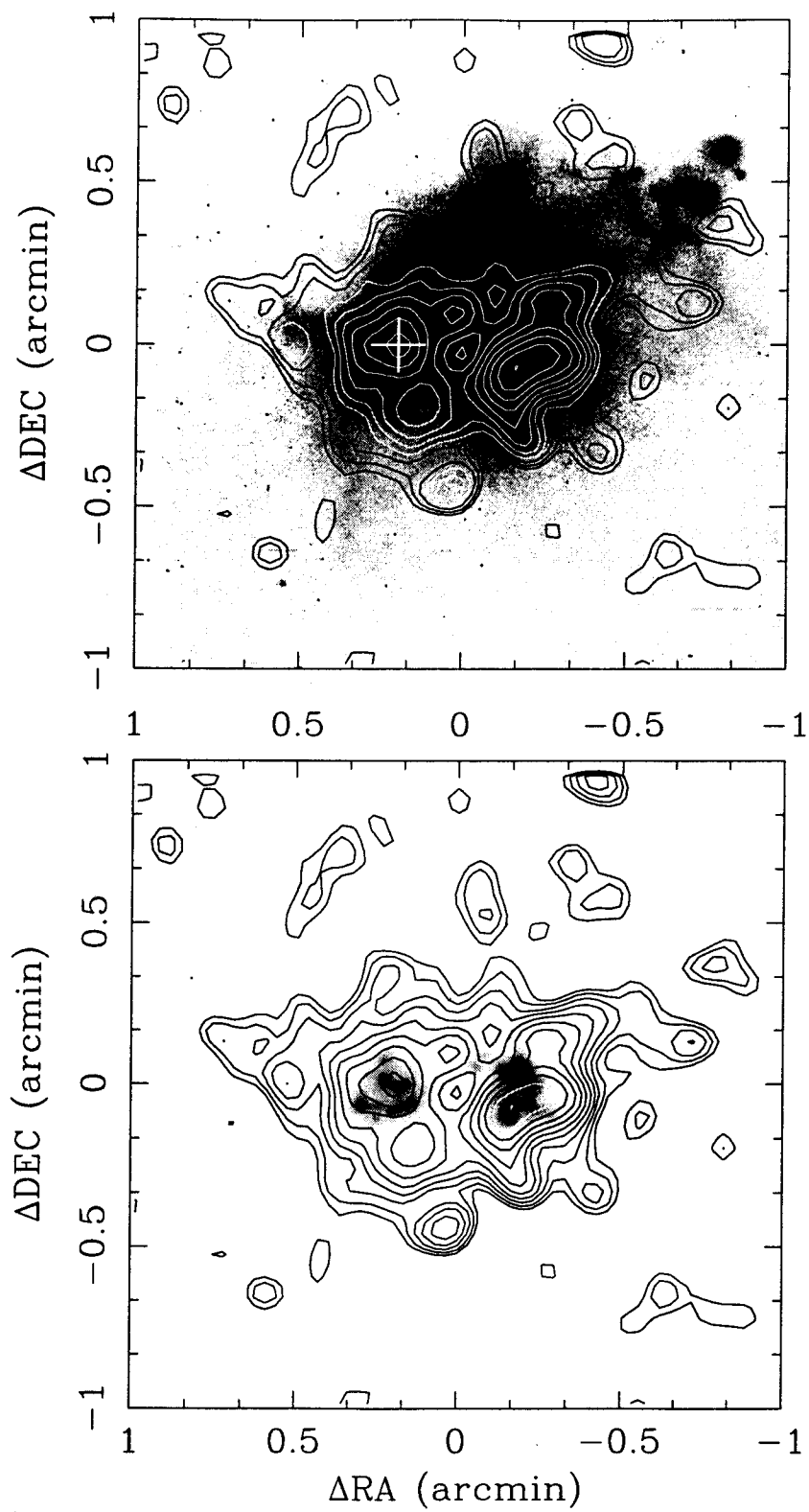
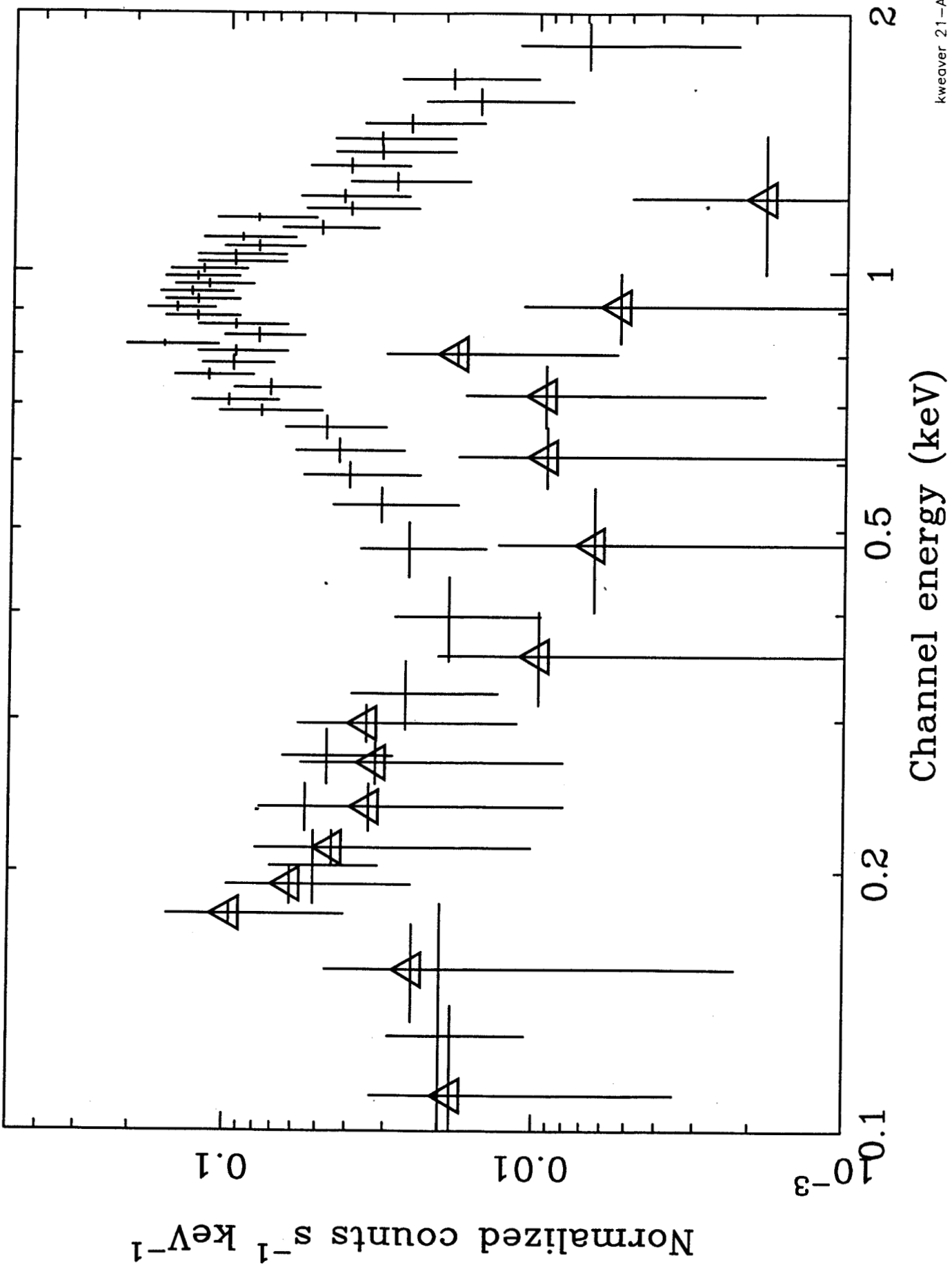


Fig. 3



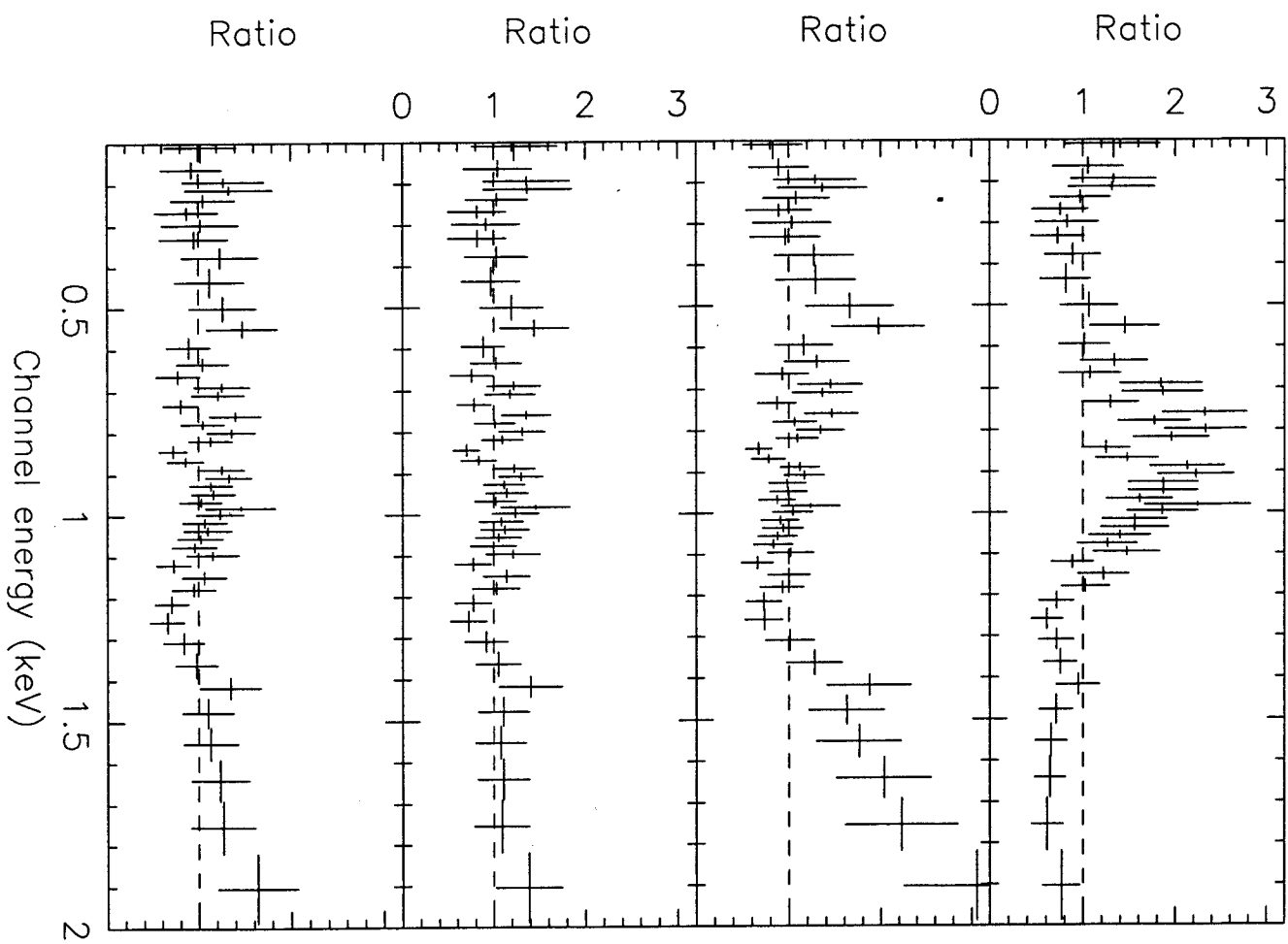
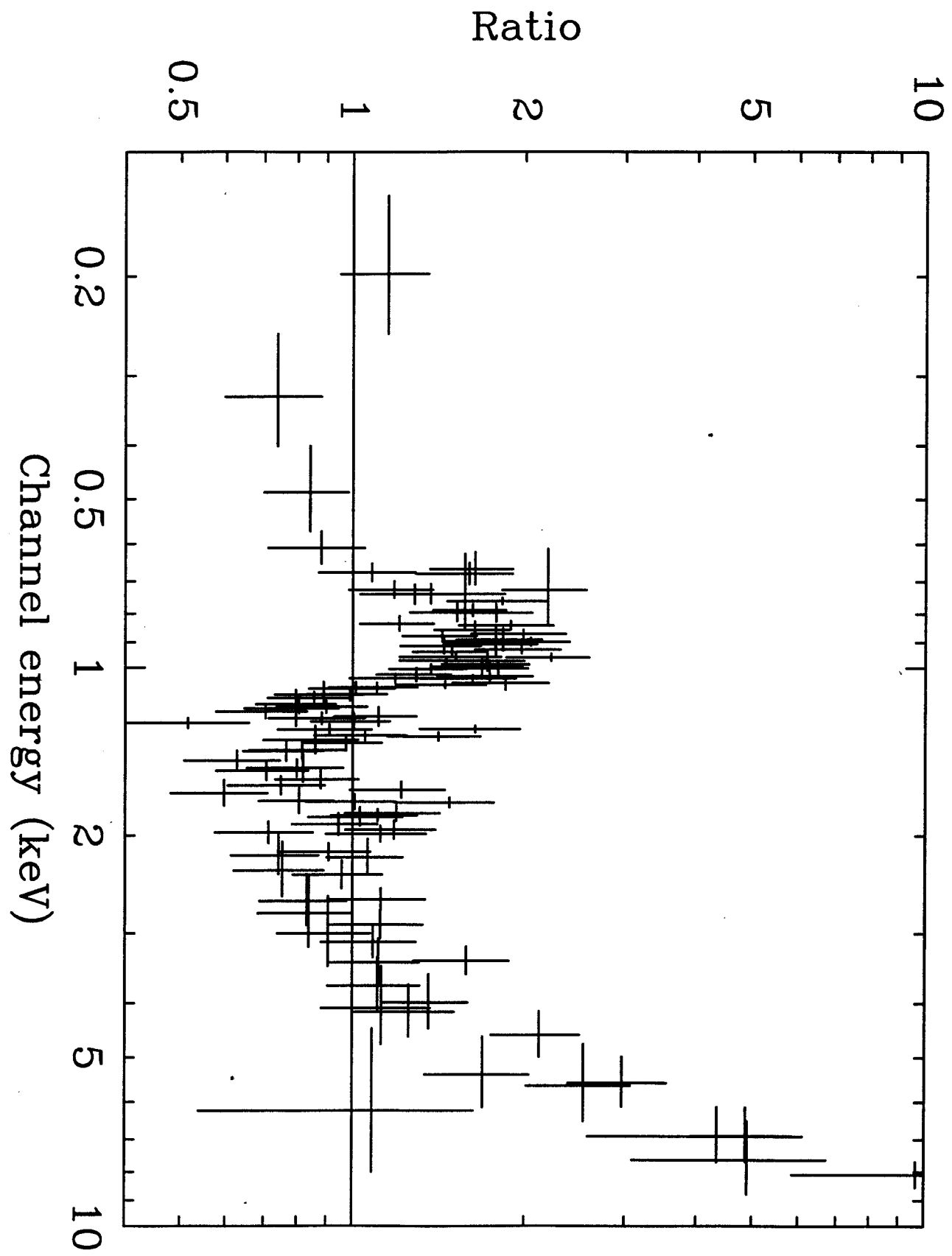
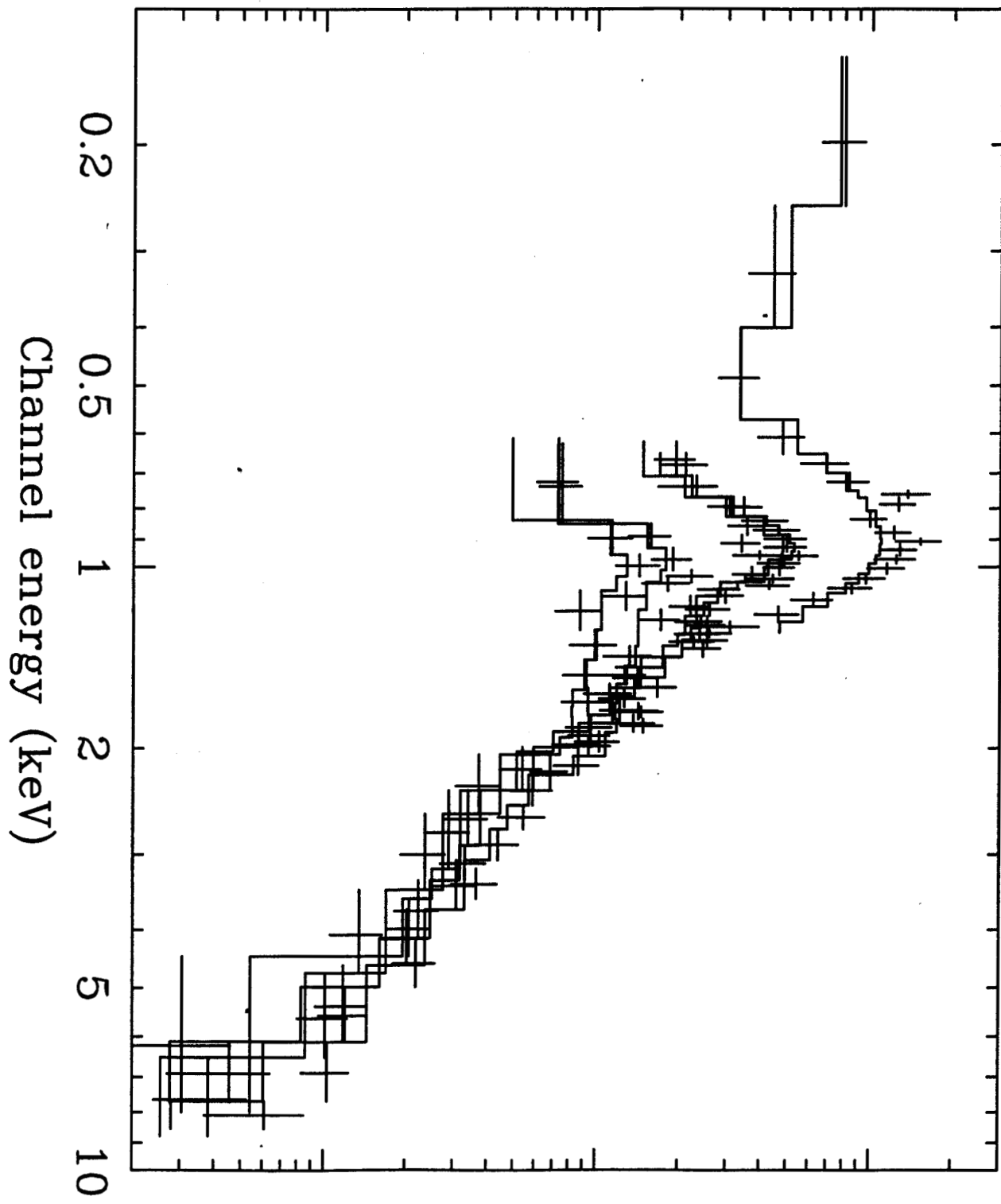


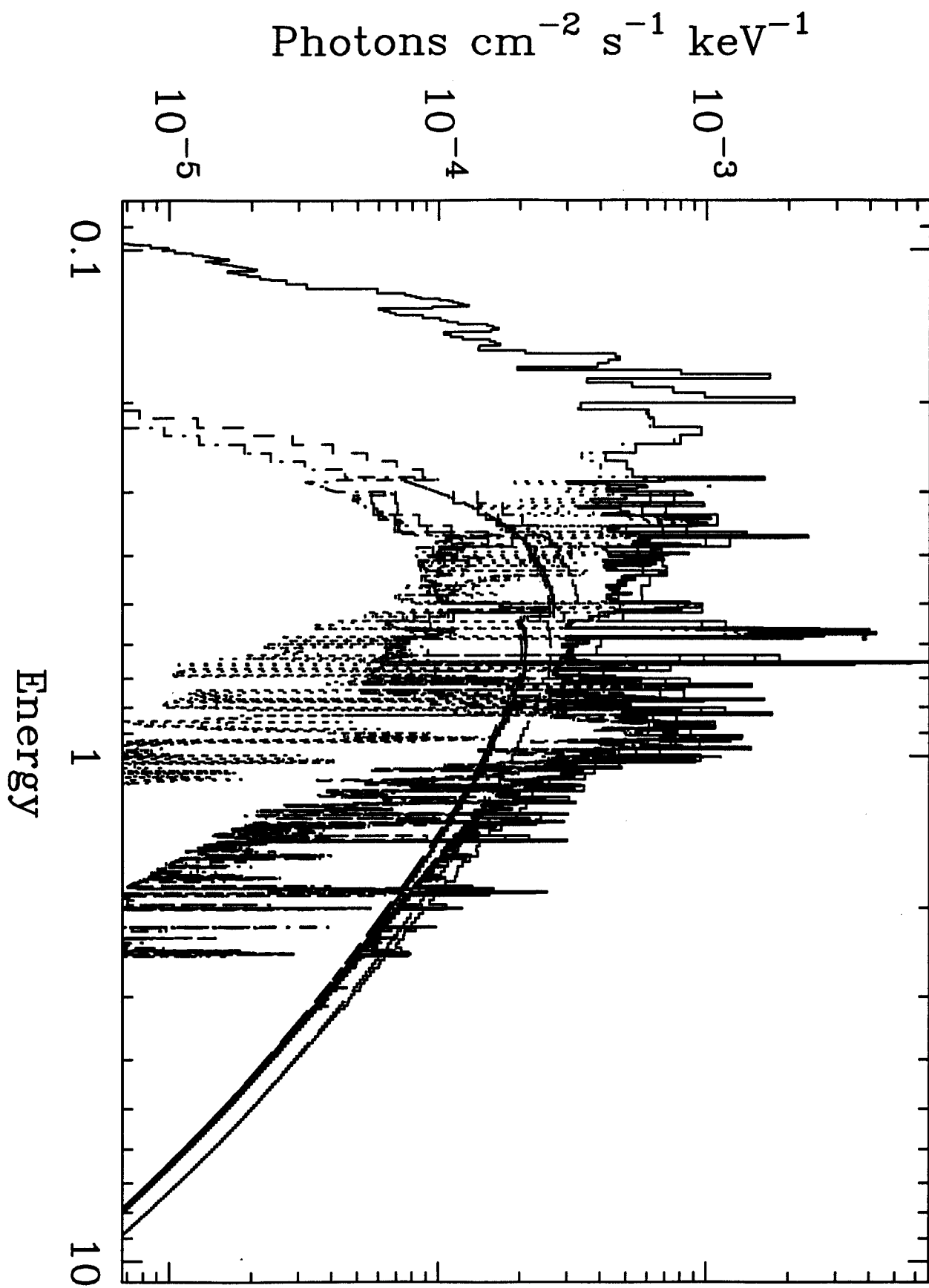
Figure 4

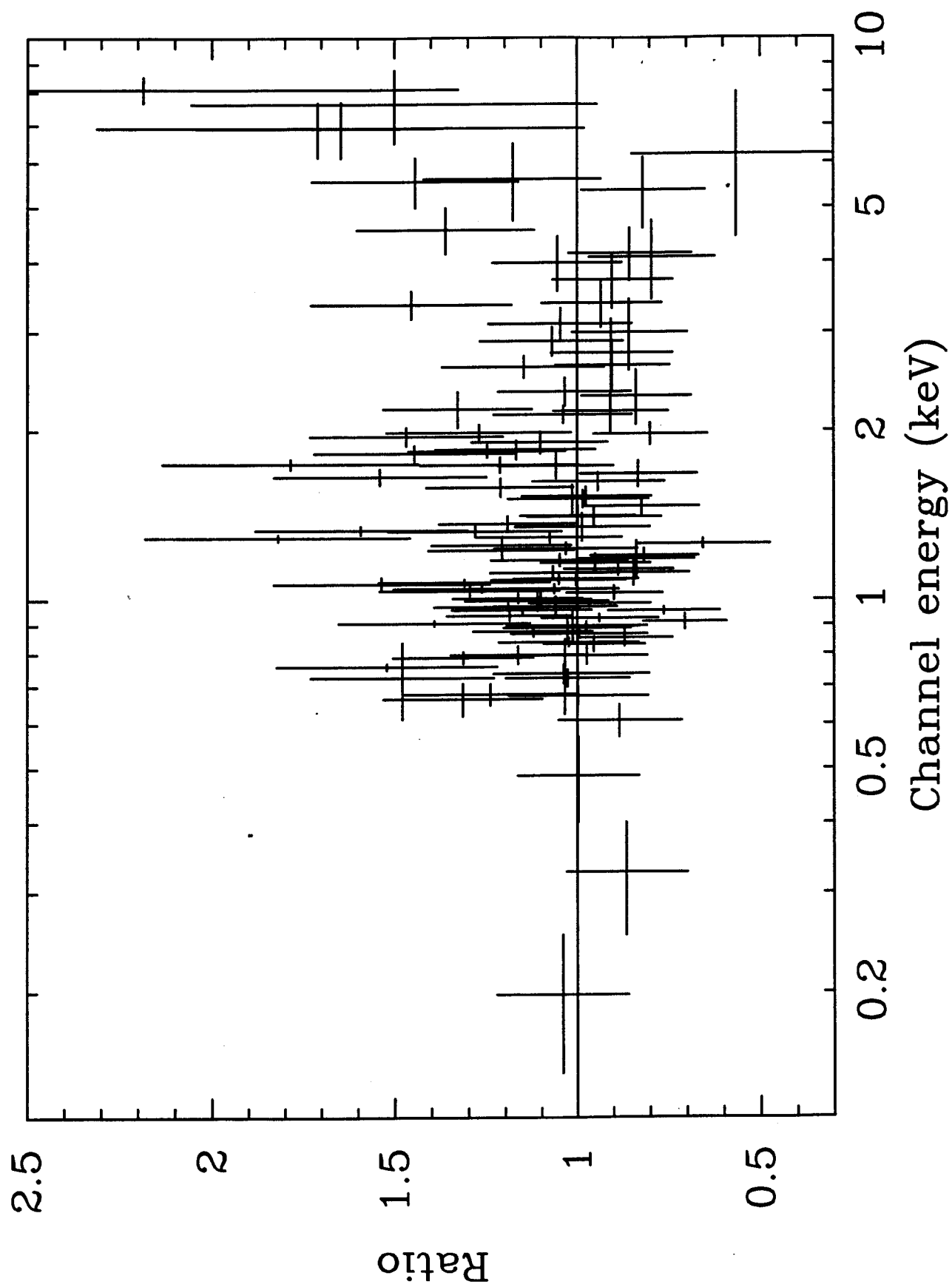


Normalized counts $\text{s}^{-1} \text{keV}^{-1}$

0.1
0.01
 10^{-3}







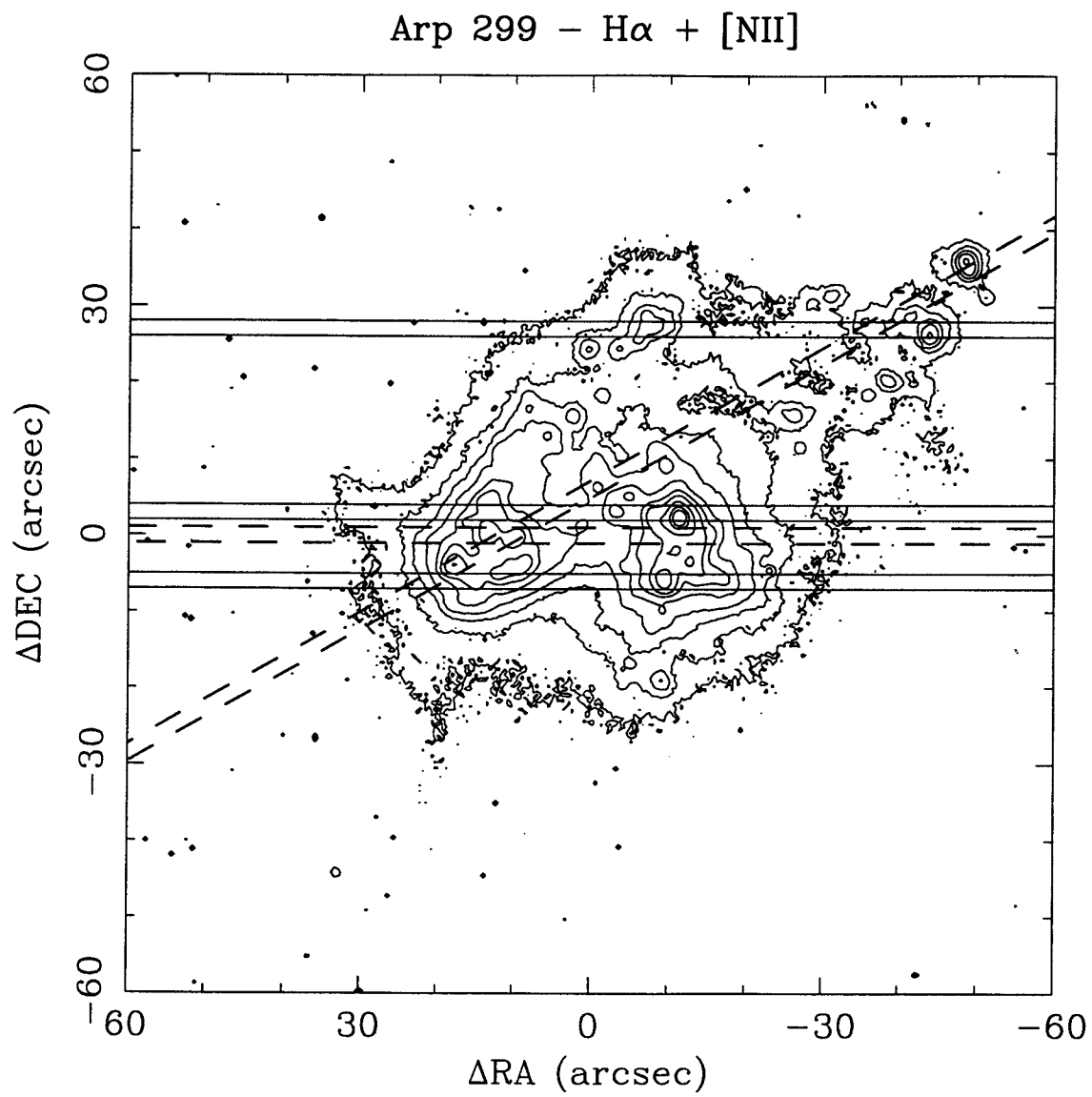


Fig. 10

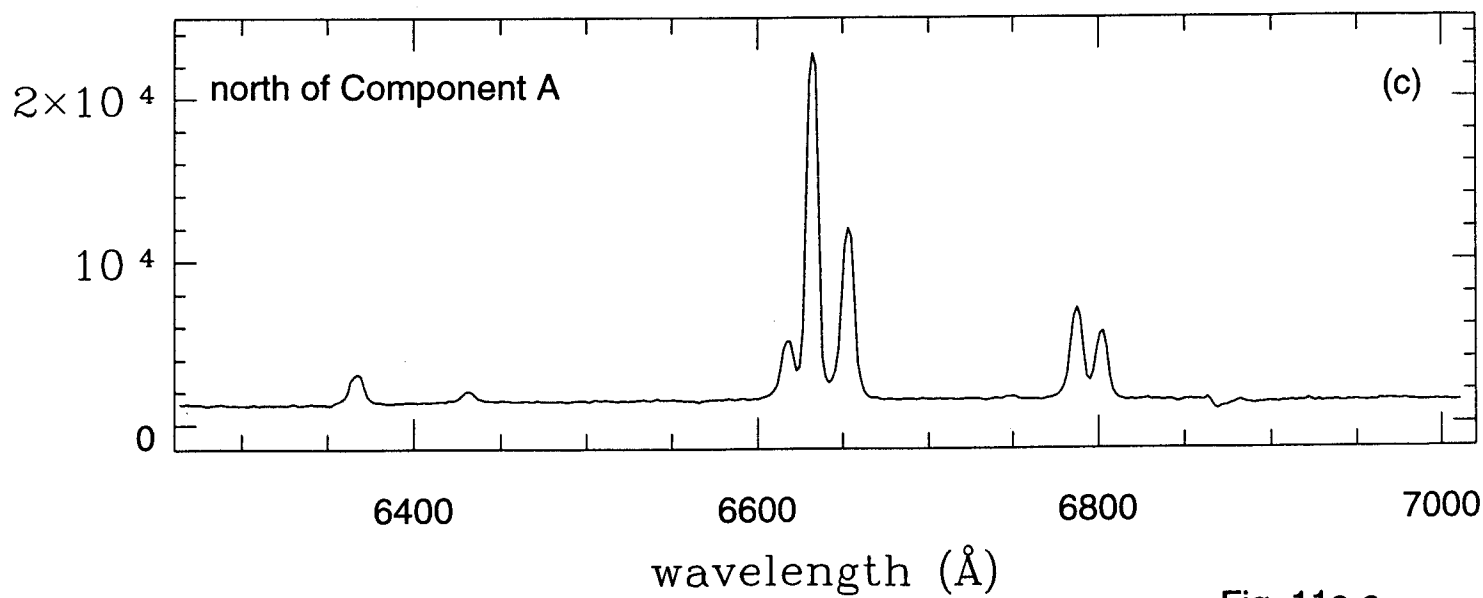
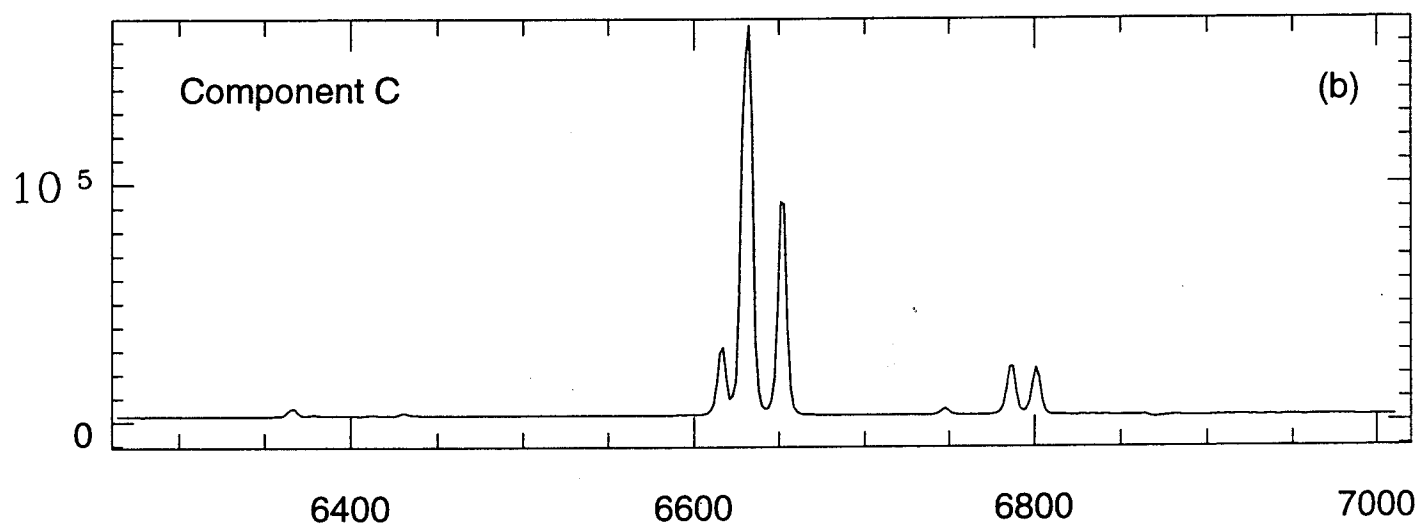
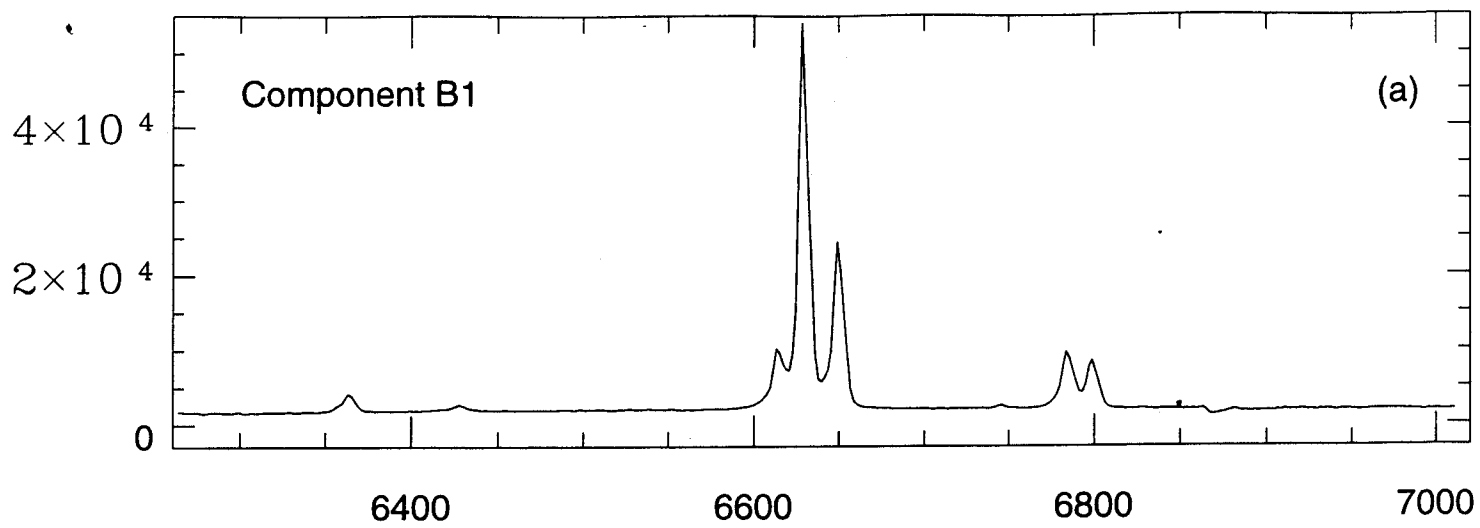


Fig. 11a-c

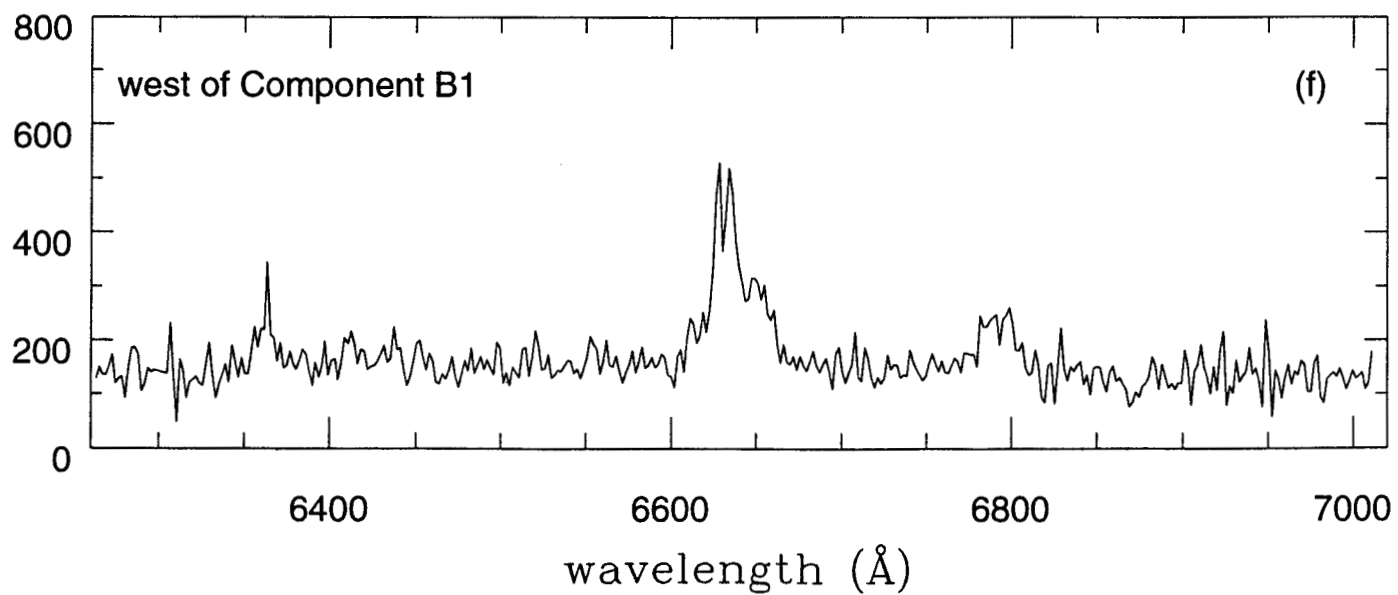
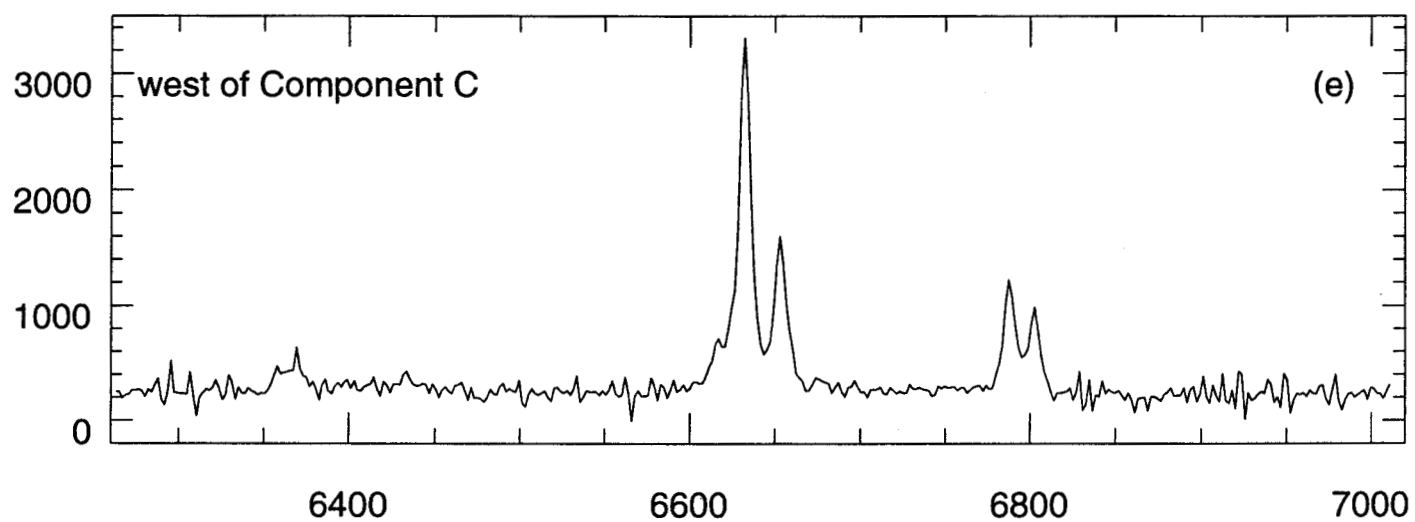
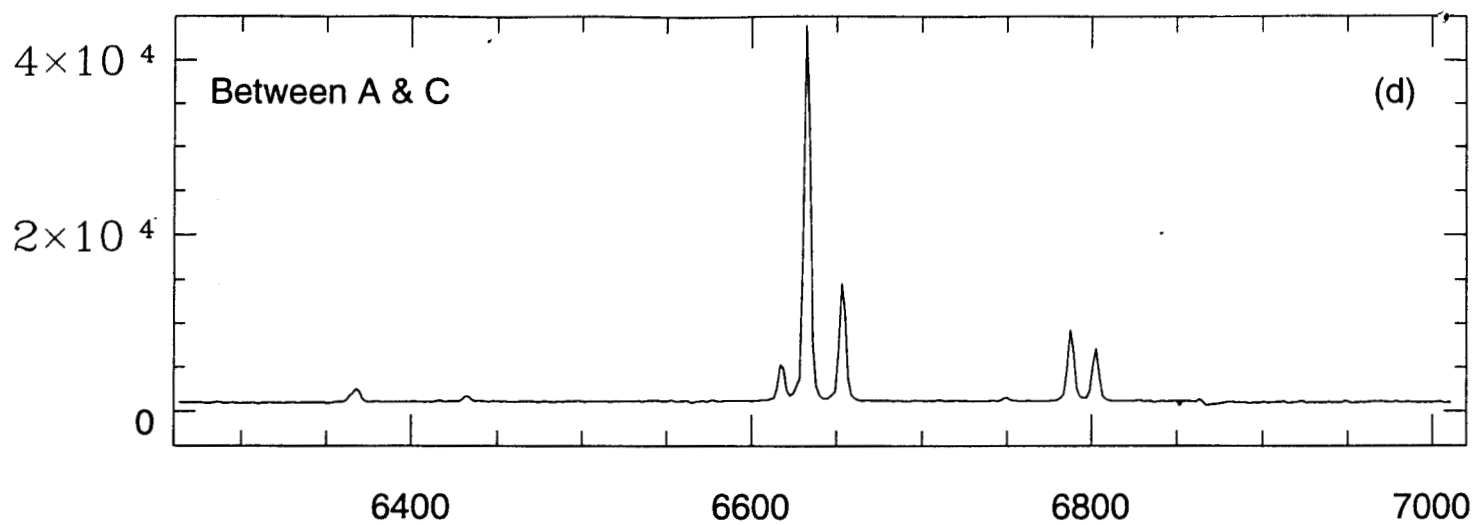


Fig. 11d-f

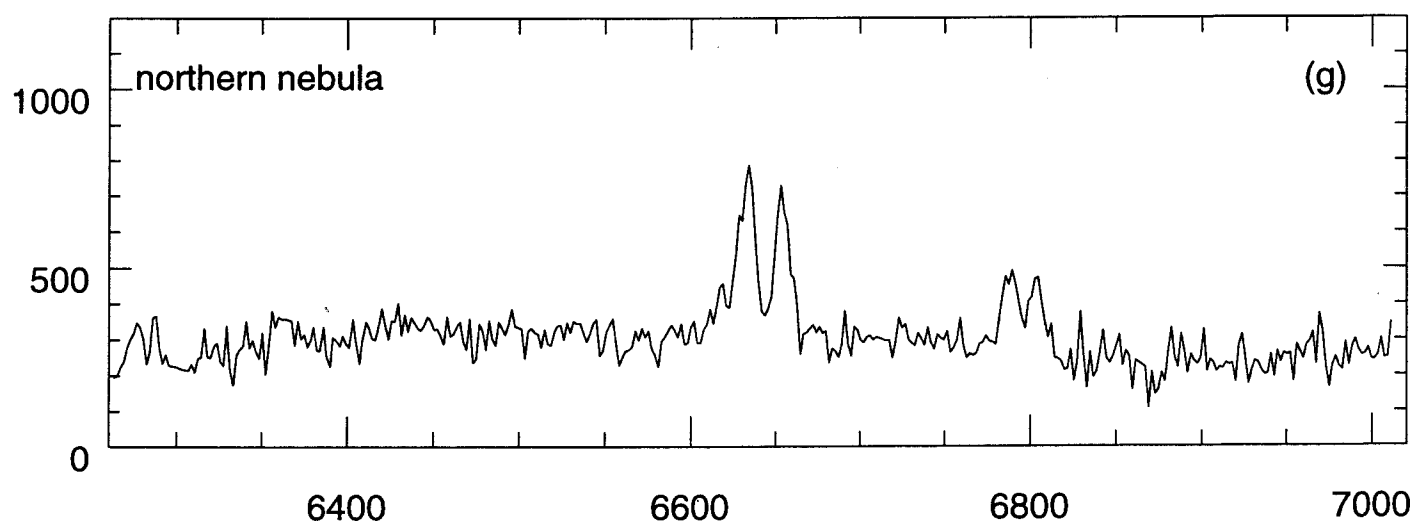


Fig. 11g

